HIGHLY EFFICIENT INFRARED PHOTODETECTORS BASED ON PLASMONIC METAMATERIALS AND VANADIUM DIOXIDE

By

Kyle Benjamin Zufelt

Thesis

Submitted to the Faculty of the

Graduate School of Vanderbilt University

in partial fulfillment of the requirements

for the degree of

MASTERS OF SCIENCE

in

Interdisciplinary Materials Science

December 2014

Nashville, Tennessee

Approved:

Jason G. Valentine, Ph.D.

Sharon Weiss, Ph.D.

ACKNOWLEDGMENTS

I would like to thank by name a few of the many people without whose collaboration and support this thesis would not have been possible. I would like to thank Dr. Jason Valentine, whose experience, foresight, and intuition provided the foundation and scaffolding of this work. I would also like to thank Dr. Sharon Weiss and Dr. Richard Haglund for their advice and support throughout my time at Vanderbilt. I would like to acknowledge the contributions of fellow students Hiram Conley, Robert Marvel, Kent Hallman, and Christina McGahan for their advice and assistance; and my lab mates: Parikshit Moitra, Yuanmu Yang, Wei Li, and Wenyi Wang, for sharing their time and resources to facilitate my research.

The fabrication and characterization of the devices in this work would not have been possible without the support of the VINSE staff: Dr. Anthony Hmelo, Dr. Ben Schmidt, Dr. Bo Choi, and Dr. Dmitry Koktysh. This research was financially supported by generous assistance from Vanderbilt University, and in particular the VINSE fellowship, the IMS program, and the Mechanical Engineering department.

Finally, I am indebted to my wife, Anneliese Zufelt, who made my brief periods of time at home manifestly more enjoyable, and who I repaid by boring nearly to death with riveting accounts of my research progress.

TABLE OF CONTENTS

Page

LIST OF TABLES

LIST OF FIGURES

Figure Page

CHAPTER 1

Introduction

1.1 Review of Infrared Detector Technologies

Highly sensitive infrared photodetection is an enabling technology for spectroscopy, astronomy, illegal weapon and drug detection, and many other areas of scientific and commercial interest[1,2]. In this chapter, we review the development and current state of the art in infrared photodetection. We will discuss the limitations and difficulties inherent to current photodetector designs, and review several topics in materials science and optics which can potentially be combined to improve upon the sensitivity of current generation IR photodetectors.

Infrared radiation refers to the region of the electromagnetic spectrum with wavelengths between approximately 700 nm (430 THz) and 1 mm (300 GHz). This band covers over 10 octaves of frequency, and includes the vibrational bands of many molecules, blackbody radiation from many living creatures, and telecommunication bands in optical fibers. Infrared detectors have existed for over 200 years, and are ubiquitous, with a wide range of sensitivities, in applications ranging from TV remote controls to night vision goggles. The earliest infrared detectors were crude thermometers which absorbed some fraction of incident infrared light, and used the subsequent temperature change to generate a visible signal, such as an increase in the volume of a mercury sample. Many modern detectors convert the absorbed light into a measurable electrical signal, which allows for more accurate measurement and facilitates subsequent data analysis. Many cost-sensitive applications rely on

bolometers, in which a temperature-dependent resistance change is measured to determine the intensity of absorbed light[3]. This resistance change can occur in a metal (Au, Al, Ti, etc.) or semiconductor (VO_x, Si, etc.) Despite a number of advances in materials and design since their development in the 1800's, bolometers often suffer from very low efficiencies, which preclude their effective use in many of the applications discussed above.

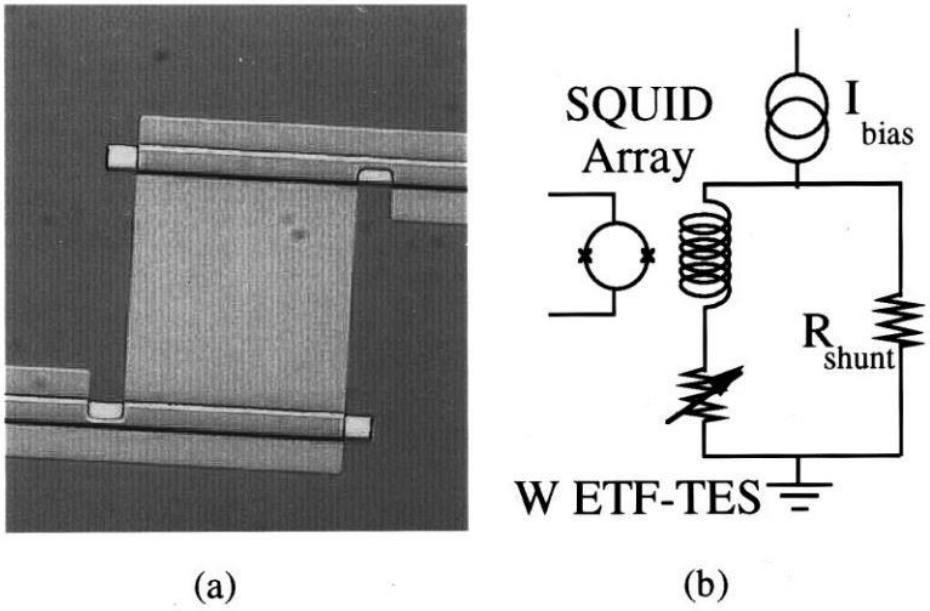

Figure 1.1 a) Electron micrograph of a tungsten superconducting transition edge sensor with an external quantum efficiency of ~10% at 1 μm. b) Diagram of circuit used for electrical read-out of detection signal. From reference 4.

The state of the art in sensitive infrared detection includes a number of geometries based on superconductors or other materials which require cryocooling to operate efficiently[5]. One such design is the transition edge detector, which operates by holding a superconducting material just below the critical superconducting transition temperature[4]. In an ideal device, when a single photon is absorbed, the subsequent

increase in temperature causes the superconductor to switch out of its superconducting state, which is detected as a dramatic and instantaneous increase in resistance. Figure 1.1a shows an image of a typical transition edge detector, along with a circuit diagram showing the effective behavior of the device. While these devices are capable of near-unity internal efficiencies, they are not capable of photon counting, require costly and bulky cryocooling equipment, and have very low detection rates due to the need to restore the device to a superconducting state between detection events. Superconducting devices can also suffer from “latching” behavior, in which joule heating, due to increased resistance in the device after a detection event, continues to heat the device and prevent a return to the superconducting state until the current is stopped. Another superconducting geometry which has recently been explored in the literature is the superconducting nanowire single photon detector (SNSPD)[6]. In this device, a superconducting circuit is cooled to well below the transition temperature and a large current is induced in the circuit such that the critical current density is nearly exceeded. In an ideal device, a single absorbed photon induces an additional current which is sufficient to induce a localized region of the superconductor to switch into a resistive state. The remaining cross sectional area of the superconducting wire is thus reduced, and the critical current density is exceeded, causing the whole device to switch into a resistive state. While these, and other, superconducting devices can potentially be switched by a single absorbed photon, these devices are often not highly absorptive, and thus suffer limitations in external quantum efficiency (EQE), which is defined as the ratio between the number of excited carriers and the number of incident photons. One area of current photonics research involves investigating ways to enhance absorptivity

in these devices[7]. Figure 1.2 shows a diagram of one such enhanced SNSPD which achieved 50% higher absorption due to incorporation of a resonant microcavity structure.

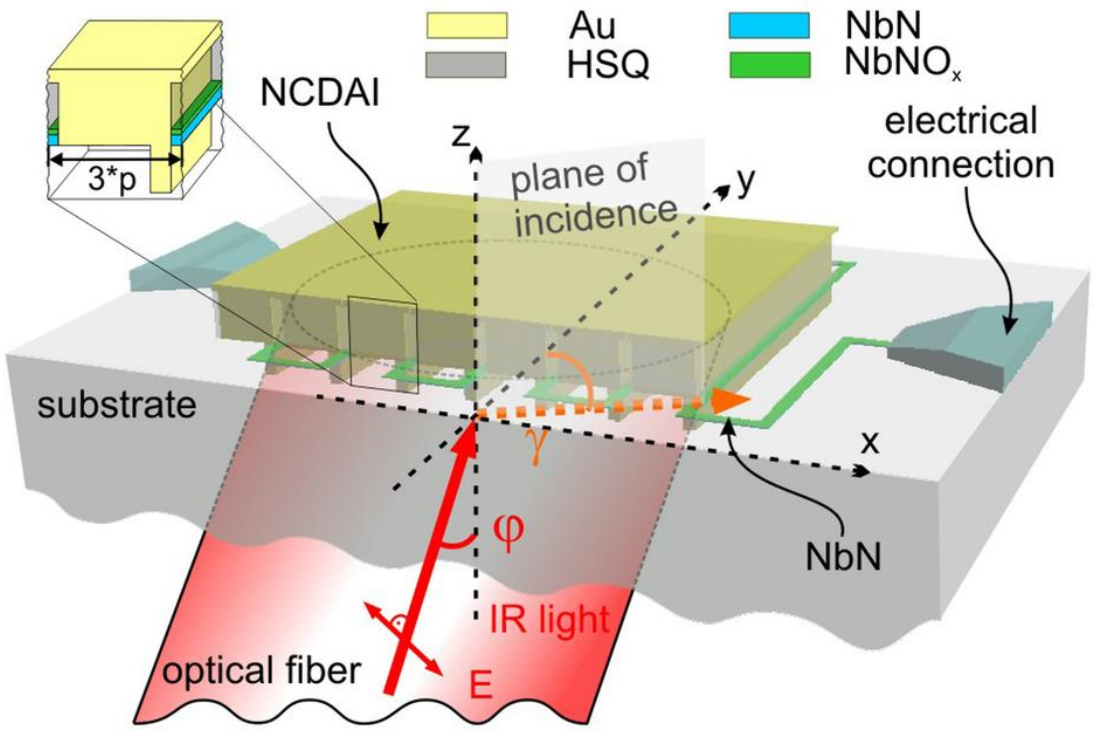

Figure 1.2 – Schematic of a superconducting nanowire single photon detector (SNSPD) with an integrated nanocavity that increases absorption from 60% to 90% at 1.55 μm. From reference 7.

In addition to the superconducting detectors discussed above, there is a wide range of highly-sensitive cryocooled semiconductor detectors. Semiconductor detectors rely on a material such as $In_{1-x}Ga_xAs$, which has a tunable band gap range of 0.34 eV (3.65 μm) to 1.42 eV (873 nm) that covers some portion of the IR spectrum[8]. In any semiconductor detector, light with an energy equal to or greater than the band gap of

the semiconductor can be absorbed to generate an electron-hole pair. One significant contributor to the dark count rate, or noise level, of a semiconductor detector is random excitation of carriers due to thermal fluctuations. At room temperature, the average energy of thermal fluctuations is equal to

$$k_B T = 8.62 * 10^{-5} \frac{eV}{K}(300K) \cong 26\, meV$$

which in an InGaAs detector corresponds to noise levels on the order of 1 nA/cm^2. As the thermal noise contribution falls off linearly with cooling, many semiconductor-based IR detectors are cooled either by thermoelectrics, for low sensitivity operation, or cryocooling apparatus, for high sensitivity operation[9]. In order to collect the electron-hole pairs in a semiconductor detector, a reverse bias is applied such that there is a net force on excited carriers, but a minimal dark current due to the built in barrier voltage. One device geometry which increases the sensitivity of a semiconductor detector is the avalanche photodiode (APD)[10]. In this configuration, the reverse bias applied to the detector is so high that the kinetic energy imparted to excited carriers by the voltage is sufficient to generate a new electron-hole pair in a process known as impact ionization. Figure 1.3 demonstrates the relationship between reverse bias voltage and gain in a superlattice APD structure. While increasing reverse bias can provide internal current gain as high as 1000, the gain results in slower detection times due to the tendency of detectors to produce “afterpulses”, and as the gain also amplifies noise sources APDs are less commonly utilized at infrared wavelengths due to lower achievable sensitivities[11,12]. Semiconductor detectors can require very complicated fabrication, particularly for multilayer quantum well devices such as the device shown in Figure 1.3, and they can also suffer from low EQE.

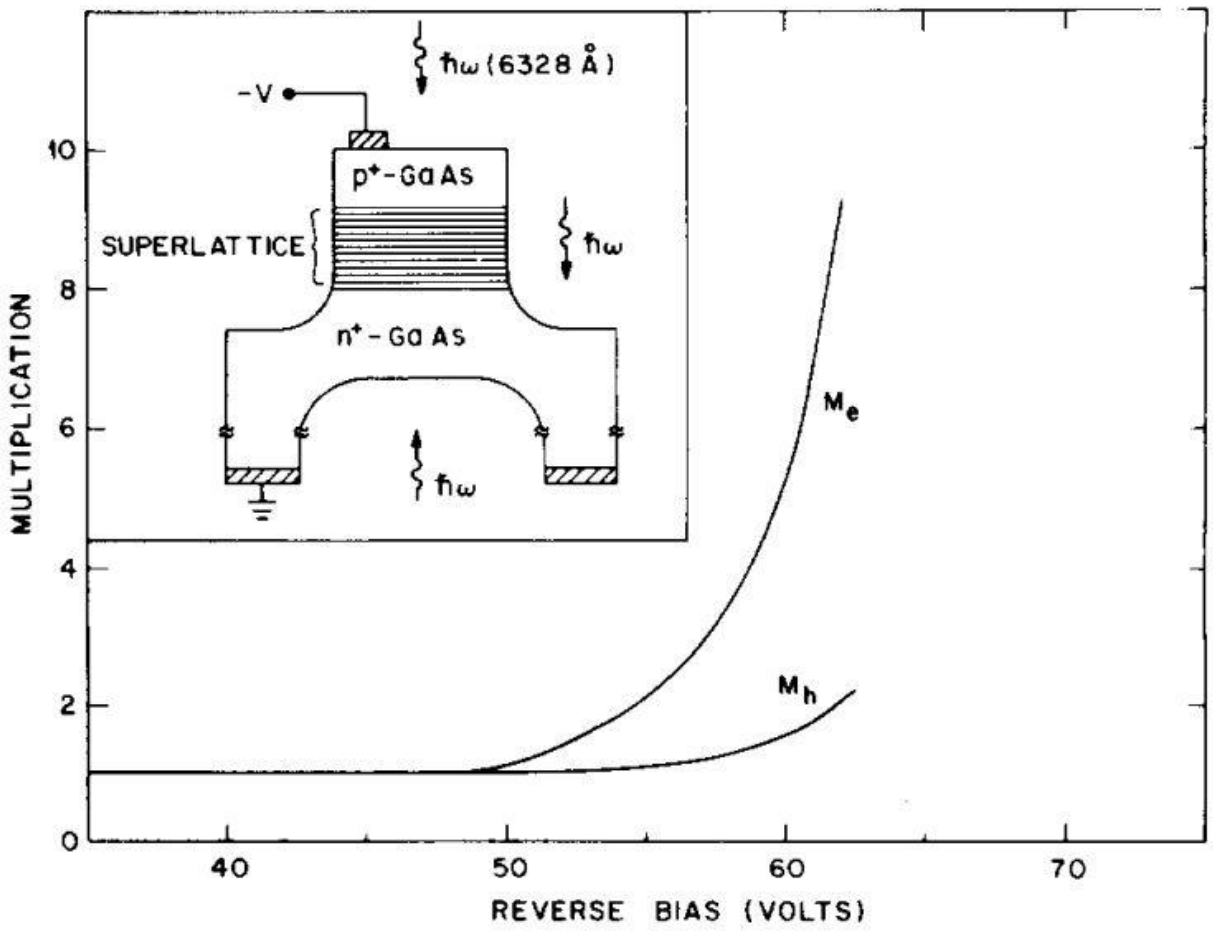

Figure 1.3 – Electron and hole gain vs voltage of a superlattice APD showing gain factors as high as 10 at 1.3 μm. Inset provides a diagram of the device with 50 alternating layers of AlGaAs and GaAs. From reference 10.

One final detector geometry which we will consider is the photomultiplier tube (PMT)[12]. While this device predates the semiconductor APD discussed above, it is in many ways superior, and is the detector of choice in many high sensitivity applications. In a PMT, an absorbed photon provides enough energy for an electron to tunnel through a vacuum between two metal plates. A large enough voltage potential between a series of these metal plates results in impact multiplication of an excited carrier by a factor of up to 10^8. PMTs are capable of single photon detection and ultra-fast detection speeds,

however, like the APD they are limited to operation at wavelengths below about 1 μm, as below this limit a rapid increase in thermionic emission increases the dark current and can easily destroy a detector. While other device geometries have been investigated[11,14,15], these devices represent the bulk of the commercial market in infrared photodetectors.

1.2 – Metamaterials and Plasmonic Enhancement

One potential route to increasing infrared photodetector efficiencies involves recent advances in the field of plasmonics[16,17,18,19]. Plasmonics refers to the study and development of devices which are designed to achieve resonant coupling between electromagnetic radiation and the electrons in a material. The quasiparticle used to describe this coupling is known as a plasmon, and these particles can exist at metal-dielectric interfaces. The frequency of plasmons is proportional to the plasma frequency, ω_p, of electron oscillations in a material

$$\omega_p \propto \frac{n_e}{m^*}$$

where n_e is the electron density and m* is the effective electron mass. Until recently, the frequency of plasma oscillations achievable in a device fabricated by top-down methods was limited by the available bulk materials. However, as we shrink the dimensions of a metal particle to nanometer dimensions, we can quantize the number of available electron states in the particles periodic potential and tune the effective electron density within the range of values less than the bulk value. Furthermore, by creating features with dimensions comparable to the wavelength of interest, surface plasmons can be directly excited by scattering off of the resonator, without the need for complicated prism

coupling or diffraction grating methods that are necessary for momentum matching at bulk metal-dielectric interfaces. Historically, this effect has been harnessed to produce colored glass by incorporating various sizes of gold and silver nanoparticles, but the role of nanotechnology in these applications was not understood until recent characterization by electron microscopy[20]. While there are many interesting plasmonic effects that have been observed and which are receiving continued attention, plasmons suffer from high loss at near-IR and higher frequencies due to the large imaginary component of the metal's permittivity associated with a decrease in electrical reactivity near the plasma frequency[21].

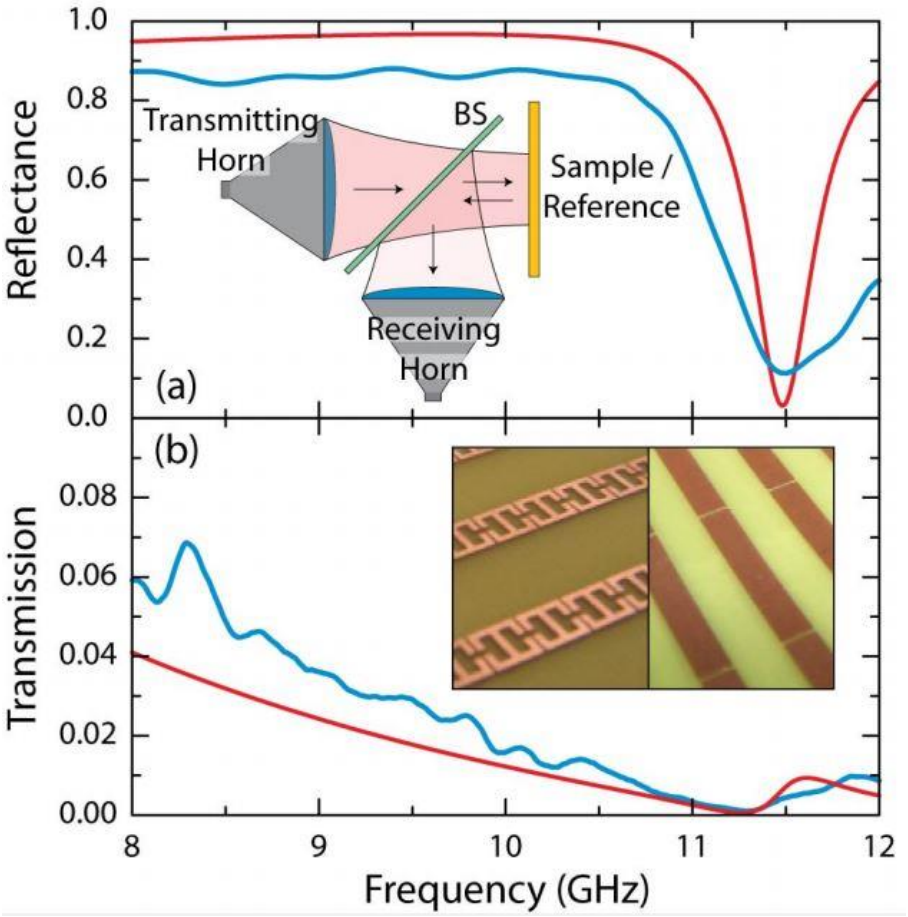

Figure 1.4 – Simulated (red) and experimental (blue) reflectance and transmission of the first metamaterial perfect absorber with a peak absorbance of 88% at 11.5 GHz (26 mm). Inset shows images of the copper antenna layer (left) and cut-wire back plane (right) with FR4 as the dielectric. From reference 24.

Another promising route to achieving highly sensitive room-temperature IR detection involves recent advances in metamaterials, materials composed of artificial "atoms" which can achieve optical properties that are not found in nature[22,23]. As long as these "atomic" unit cells are much smaller than the wavelength of incident light, the behavior of the light will be defined by effective optical properties of the composite material instead of the properties of discrete elements or materials in the device. One interesting property that can be achieved in metamaterials is unity, or "perfect",

absorption. Metamaterial perfect absorbers (MPA) were first proposed by Padilla and Smith in 2008[24]. Figure 1.4 provides information on the theoretical and experimental optical properties of their proof-of-concept device, which achieved 88% absorption. Because metamaterial theory provides a design tool for manipulating both the real and imaginary parts of the electric permittivity and magnetic permeability of a structure, we can build a structure with overlapping, impedance-matched electric and magnetic resonances. Optical impedance is defined as

$$Z_i = \sqrt{\frac{\mu_0 \mu_r}{\varepsilon_0 \varepsilon_r}}$$

where μ_0 is the vacuum permeability, ε_0 is the vacuum permittivity, μ_r is the relative magnetic permeability, and ε_r is the relative electric permittivity. Impedance determines the magnitude of reflection at the boundary between two materials according to the following equation,

$$R = \left(\frac{Z_2 - Z_1}{Z_2 + Z_1}\right)^2$$

where in our case Z_1 is the impedance of air and Z_2 is the impedance of the MPA. When the two materials are impedance matched ($Z_2 = Z_1$), $R = 0$ and the wave couples completely into the material. In air, $\varepsilon_r \cong \mu_r \cong 1$, which means that to achieve perfect coupling we need $\varepsilon_r \cong \mu_r$ in our material. However, at high frequencies most materials have $\mu_r \cong 1$ and $\varepsilon_r > 1$, and it is difficult to achieve impedance matching. Because metamaterials allow for independent control of the relative permittivity and permeability, we can achieve impedance matching even at high frequencies. In general, MPAs

control permittivity by exciting an electric resonance in an antenna layer (the copper split rings in Figure 1.4), and permeability by exciting a magnetic resonance due to coupling between the antenna layer and a reflective back plane or wire array (the cut wires on a FR4 dielectric layer in Figure 1.4). In addition to eliminating reflection through impedance matching, a reflective back plane eliminates transmission, and loss occurs in the metal or dielectric, allowing for total absorption of light in a small volume of material at a particular wavelength. Instead of seeking to minimize plasmonic losses, MPAs seek to obtain functionality by maximizing loss. Most MPA investigations ignore the heat generated by plasmonic losses in the absorber, and while this is sufficient for applications such as a beam blocker or a telescope coating, the loss can be harnessed to provide functionality, particularly if we were able to localize the losses to maximize a local temperature increase.

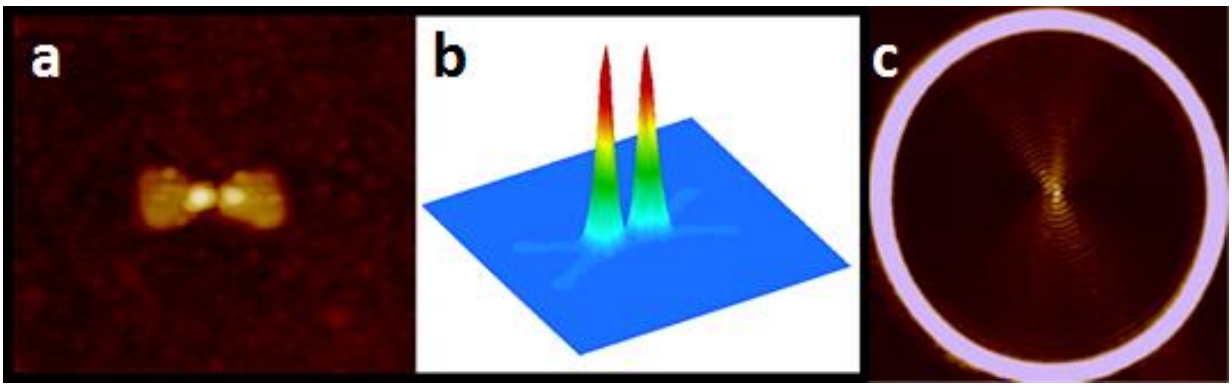

Figure 1.5 – AFM scan of nano bowtie antenna (a), with highly localized intensity enhancement demonstrated by residual photoresist exposed by plasmonic lithography, and confirmed by FDTD near-field intensity profile in antenna plane (b). A plasmonic lens (c) allows focusing through interference of surface plasmons, as demonstrated by near-field optical scanning microscopy. From references 25 and 26.

In particular, we here consider two geometries studied previously: a MPA geometry consisting of periodic bowtie antennas[25], and a plasmonic lens structure[26]. A bowtie antenna is a two-dimensional projection of a biconical antenna, a broadband design which was first proposed in 1898 by Sir Oliver Lodge, only 12 years after the experimental confirmation of electromagnetic radiation by Heinrich Hertz. As bowties are scaled to optical wavelengths, plasmons are generated in the material, and focused to the gap between the antennas such that they can provide very high intensity enhancement and localized loss in the central gap[27,28]. In Figure 1.5a, researchers coated a bowtie antenna in photoresist, and illuminated the antenna at low intensity such that the photoresist was exposed proportional to the intensity of the local electric field enhancement. After developing the photoresist, they took a surface map which experimentally demonstrates the field enhancement in the gap between antenna halves. Figure 1.5b further shows a computational model of the field profile.

In addition to a metamaterial perfect absorber geometry utilizing a repeated unit cell containing a bowtie antenna, a hybrid device in which a single bowtie antenna is located at the center of a plasmonic lens has been demonstrated. A plasmonic lens is a structure which allows focusing of surface plasmons by controlling interference between individual electron density oscillations[29]. Figure 1.5c shows a near-field scanning optical microscopy (NSOM) scan of a single-ring plasmonic lens, with periodic intensity fringes demonstrating the interference effects between plasmons generated at different points along the ring. When the difference in diameter between successive concentric rings is equal to the target wavelength, surface plasmons interfere constructively at the center of the lens to provide intensity enhancements of ~10x. This is far less than the ~1000x

provided by a bowtie antenna, and the lens is furthermore not capable of perfectly absorbing light like the bowtie-MPA. However, by placing a plasmonic lens structure around a single bowtie antenna, we effectively multiply these enhancements, coupling a far greater area of incident light into a single antenna and potentially achieving a larger temperature change than would be possible in an array of coupled bowtie antennas.

1.3 – Vanadium Dioxide

Vanadium dioxide (VO_2) is a correlated electron material, currently used in commercial IR bolometers, which nominally undergoes a semiconductor-to-metal phase transition at 68 °C[30,31]. This phase transition occurs due to a slight perturbation in the crystal lattice geometry from monoclinic to tetragonal. This phase change has been investigated for uses in computer memory, thermochromic windows, and optical modulators, due to the extreme speed of the switching, which can take as little as 100 fs [32,33,34]. The optical properties of VO_2 change most dramatically at infrared frequencies as seen in Figure 1.6b, making it ideal for use in active IR optics. Furthermore, the resistance of VO_2 can change by up to 3 orders of magnitude upon switching[35], which allows for accurate electrical read-out of a change in temperature or electric field. Data in Figure 1.6a shows a two order of magnitude resistance change in a VO_2 film on glass, which is likely lower than has been observed in other publications due to a small average grain size and large grain size distribution. While the phase change of VO_2 can stabilize in 100 fs, the phase change is typically extended over ~5 degrees, such that a VO_2 detector would allow for photon counting functionality and rapid reset speeds. The phase change can be further extended by doping with tungsten, at the cost of decreasing the magnitude of the resistance change[36].

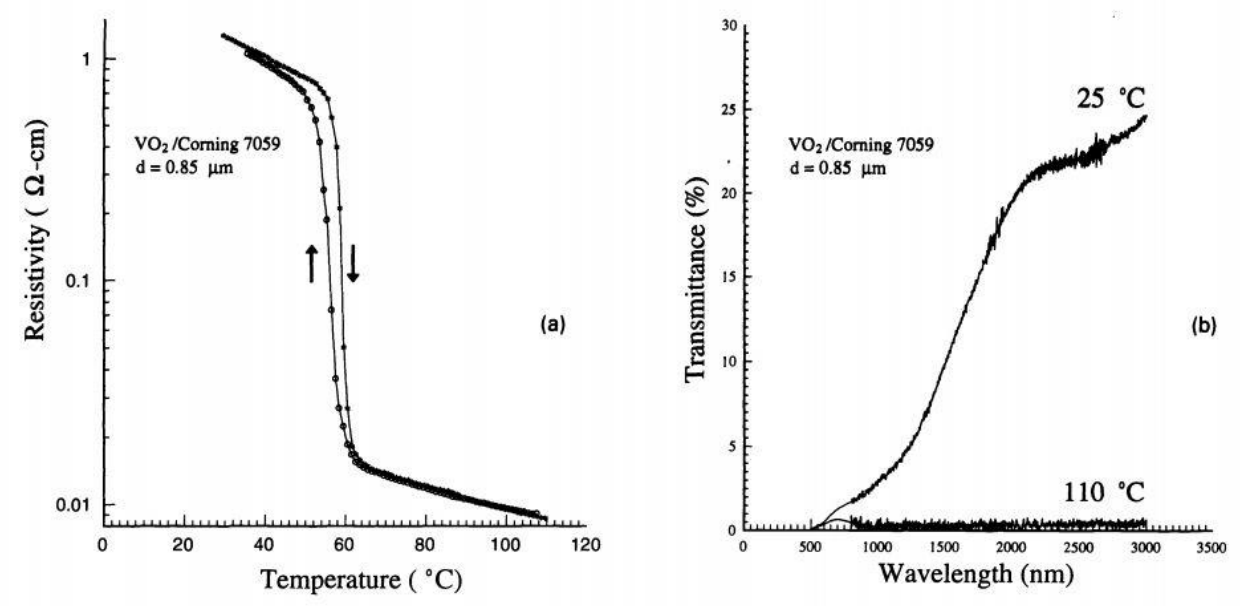

Figure 1.6 – Resistivity (a) and IR transmittance (b) of a VO_2 thin film on glass, showing dramatic changes above and below the transition temperature of 68 °C. From reference 30.

CHAPTER 2

Design

2.1 – Optical Modeling of Metamaterial Perfect Absorbers

We chose to design two bowtie antenna devices to achieve high field enhancements as seen in Chapter 1. One device consists of bowtie antennas arranged in an MPA geometry, while the other consists of a single bowtie at the center of concentric plasmonic lenses. Both of these devices will have vanadium dioxide as the active material in the field concentration zone between the two halves of the bowtie antennae. By using VO_2 as our active material, the goal is to maximize the resistance change of our devices for a given input intensity.

Both devices were designed to operate at 1.55 μm (193 THz), a zero-dispersion wavelength in quartz fiber, and thus one of the two optical telecommunications bands. The telecommunications industry nets an annual revenue of billions of dollars, and as the global demand for higher bandwidth necessitates continued conversion from electrical to optical data transmission there will also be an increased demand for sensitive near IR detectors which can operate near room temperature[37]. Designing a device which operates in the near IR also greatly facilitates experimental measurement of devices due to the readily available commercial laser and detector systems.

Both structures considered in this work were designed in Computer Simulation Technology Microwave Studio (CST MWS), a commercially available FDTD solver. Structures were designed in a three-dimensional CAD format, where individual sample

dimensions were parameterized to allow for optimization. All structures were illuminated with either waveguide ports, which were placed in the planes 1 μm above and below the structure to allow determination of absorption in the structure, or an incident plane wave, which allowed control over the intensity of illumination and thus direct determination of intensity enhancement. First, we investigated an individual bowtie antenna in an infinite vacuum to identify the spectral location and electromagnetic profile of each resonance in the structure. The dipole resonance in the antenna was identified by a strong electric field directed linearly between the antenna halves, and a corresponding rotating magnetic field. Figure 2.1 shows maps of the calculated electric field, where regions of higher field enhancement are show as more “red” in color, and perpendicular magnetic field, where out of plane magnetic field enhancement is shown by either blue or red colors depending on whether the field is currently directed out of or into the substrate. The dipole resonance produces a high field concentration between the two halves of the antenna, which is the optimal field profile for heat generation in the region where we will eventually place VO_2. It has been shown that the optimal flare angle in a bowtie antenna for maximizing the rotational magnetic field in the gap is 45 degrees and that, as plasmonic heating occurs only at the metal surface, thinner structures have a higher volumetric heat generation[39,40]. Once the dipole resonance was located in a thin, 45 degree bowtie structure, the resonance was shifted to the desired wavelength of 1550 nm by changing the size and gap width of the antenna.

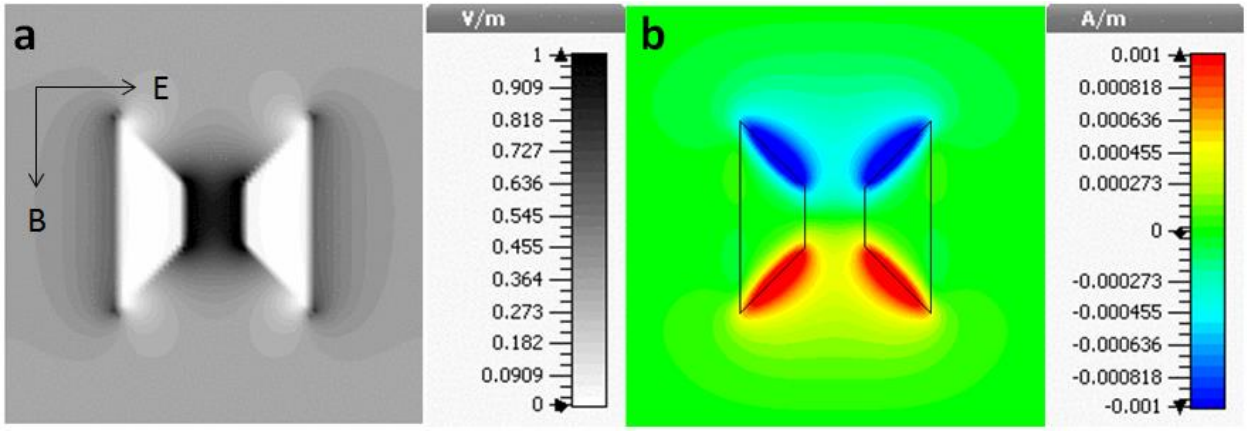

Figure 2.1 – Field profiles for gold bowtie structure in air confirm dipole resonance. Highly localized electric field (E_{abs}, a) results in strong rotating magnetic field around gap (H_z, b) which will contribute to loss when VO_2 or another lossy material is placed in close proximity. Results are normalized to a 1 V/m incident electric field polarized as shown. Note that the scales have been intentionally saturated to increase contrast. The maximum electric field concentration is 6 V/m and the maximum magnetic field concentration is ±0.01 A/m.

After a single antenna had been optimized in vacuum, we were able to use that antenna with minor changes for both the MPA and plasmonic lens geometries. For the MPA design we placed this structure on a thin film stack composed of (top to bottom): a layer of VO_2, a thin insulating dielectric layer, and a reflective back plane, all on a quartz substrate. We then tiled the bowtie in the two dimensional plane of the surface, placing electrical bus bars along the outside edges of each antenna as shown in Figure 2.2a. Thus, by applying a bias between alternating bus bar columns, we can measure the electrical resistance of the VO_2 in every gap in parallel, where

$$R_{total} = ({R_1}^{-1} + {R_2}^{-1} + {R_3}^{-1} + \cdots + {R_n}^{-1})^{-1}.$$

and R_x represents the resistance of an individual unit cell. The insulating layer prevents current leakage through the reflective back plane, and the antenna layer ensures that heating will be localized in the gaps. Thus, an incident photon is absorbed by the device, and can generate sufficient heating in the gap of one, or several, bowties to

induce localized switching in the VO_2, particularly when the VO_2 has been heated to near the transition temperature or doped to reduce the transition temperature. The resulting resistance change in a single unit cell will produce a detectable resistance drop in arrays of up to 10^6 antennas (> 100 x 100 µm active area) as shown in Figure 2.3b, assuming a resistance change of two orders of magnitude in the single switched device. By varying the period of the unit cell, we were able to optimize coupling between antennas, and by varying the thickness of the VO_2/dielectric stack, we were able to optimize the coupling between the antenna layer and the reflective back plane which supports the magnetic resonance. In our simulations, we achieved near-perfect absorption of 99.999%, as demonstrated in Figure 2.2b.

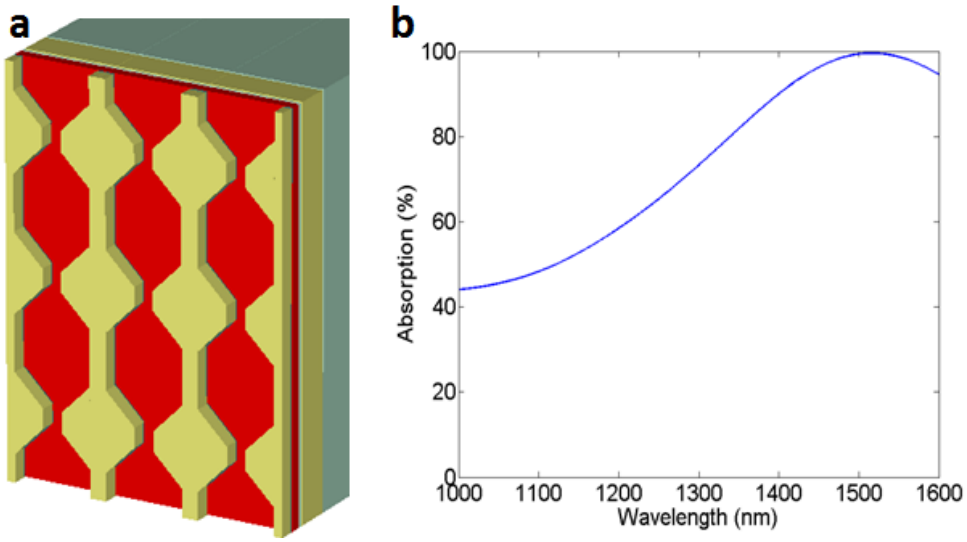

Figure 2.2 – The metamaterial perfect absorber structure (a) consists of periodically spaced bowtie antennas connected by electrical bus bars. The gap width is 50 nm, the bus bar width is 45 nm, and the x- and y- unit cell spacings are 250 nm and 350 nm, respectively. The vanadium dioxide (VO_2) is shown as a continuous red film (35 nm thick) between the top antenna layer (45 nm thick) and the insulating dielectric film (10 nm thick), with a reflective gold film (100 nm thick) underneath. The simulated absorption at 1510 nm is 99.999% (b).

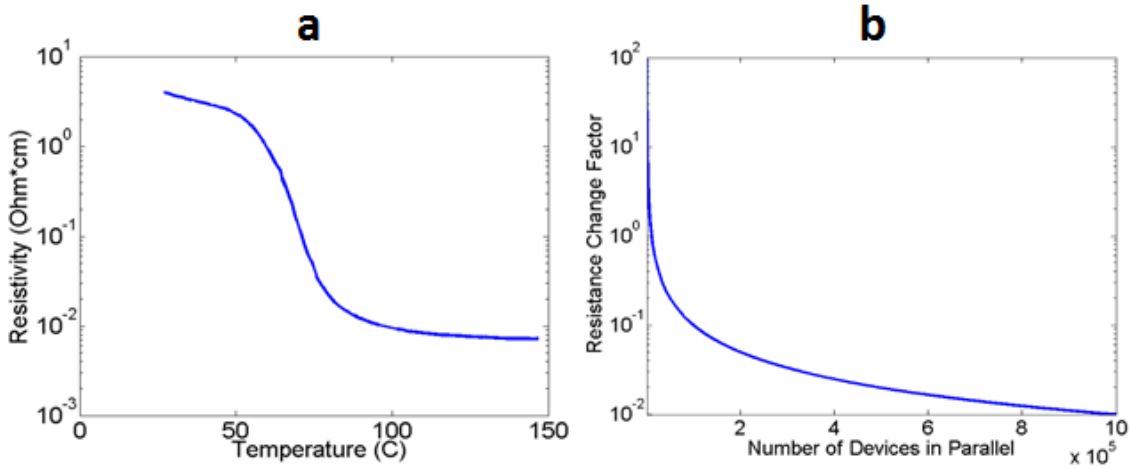

Figure 2.3 – A typical resistivity change upon switching in bulk VO_2 films is two orders of magnitude (a). Assuming this magnitude of change, even very large arrays (>10^6 devices) would produce a detectable (>10^{-2}) resistance drop upon switching of VO_2 in the gap of a single bowtie antenna (b). The resistance change factor (RCF) is given by $R_f = R_i(1 - RCF)$ where R_f is the resistance of the array after switching and R_i is the resistance of an unswitched array.

2.2 – Optical Modeling of Plasmonic Lenses

For the plasmonic lens structure, we determined the spacing of the rings by using the grating equation

$$n\lambda = d \sin\theta$$

where n is the diffraction order, λ is the scattered wavelength, and θ is the angle of incidence. Thus, to determine the appropriate spacing to achieve in-plane first-order diffraction of light at normal incidence, we can simplify to obtain

$$d = \lambda = 1550\ nm.$$

However, in addition to scattering free space light, our device needs to maximize interference effects between localized surface plasmons. Per Gauss's law, we can determine that the electric field generated by an individual ring of the lens will fall off as

d^{-2}, which tells us that a closer ring spacing will result in stronger coupling. By simulation we found that a grating period of $\frac{\lambda}{2} = 775\ nm$ produced the strongest intensity enhancements at the center of the structure by exciting a second-order resonance with strong inter-ring coupling. The diameter of each concentric ring in our design is larger than that of the next smallest ring by the reduced grating period of 775 nm. While the above derivation of grating period is only strictly correct for the simple case of a 1-D linear grating, the value is approximately the same for our more complicated structure, and parameter sweeping found no significant increase in intensity enhancement for sweeps with experimentally repeatable step sizes (>20 nm). The two free parameters left for consideration in a ring-shaped grating are the diameter of the smallest circle, D_i, and the ratio of the ring width to the ring spacing. For this structure, a small patch of VO_2 was placed at the center of the bowtie antenna, instead of the continuous VO_2 film used in the MPA geometry, and the reflective back plane was removed. Reflections at the edge of the computational volume were eliminated by using a layered boundary which was infinite in the x-y plane, but which matched the optical properties of either air or sapphire depending on which material the boundary intersected. While the plasmonic lens is not inherently polarization sensitive, the bowtie antenna imposes polarization sensitivity on the device geometry. Accordingly, in our simulations we cut the plasmonic lenses at a 45 degree angle to allow for the inclusion of electrical bus bars, as shown in Figure 2.4a. By varying the thickness and size of the VO_2 patch in addition to the previously discussed lens parameters, we were able to achieve an intensity enhancement of 500x at the center of the bowtie antenna. Figure 2.4b demonstrates

how the intensity enhancements of a plasmonic lens and bowtie antenna multiply when incorporated into a single geometry.

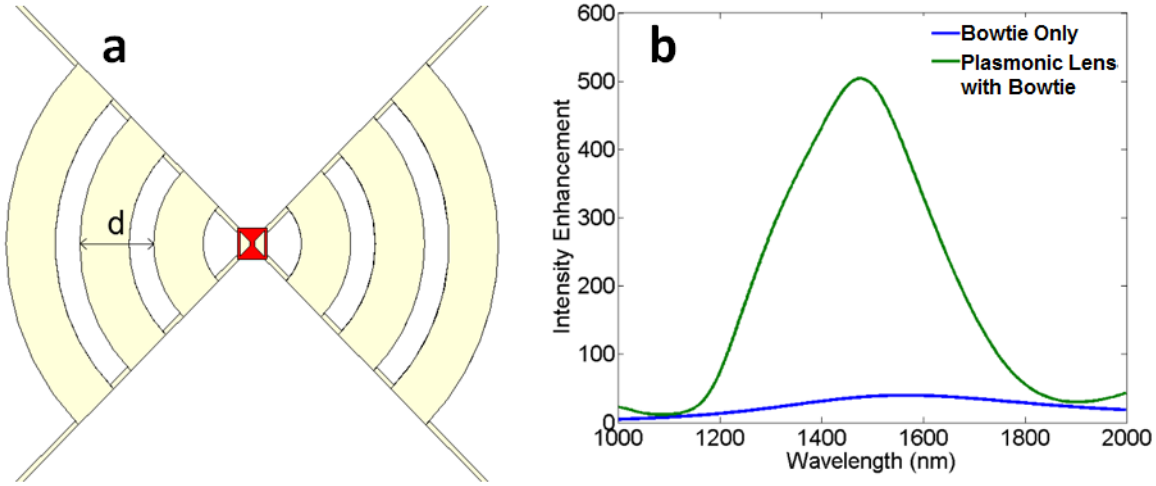

Figure 2.4 – The plasmonic lens structure (a). Vanadium dioxide is modelled as a small red square (500 nm to a side) at the center of the lens. The grating period is labeled d, and is proportional to $\lambda/_2$. Placing a series of three concentric rings around the bowtie results in a ~10 x intensity enhancement over the bowtie in free space, for an overall enhancement factor of 500x (b).

2.3 – Device Performance Modeling

It is essential when designing any photodetector to quantify the theoretical limits of performance metrics such as sensitivity, speed, and dynamic range. Thus, in addition to optimizing the optical properties of each device, we developed thermal and electrical models to provide further information necessary to these calculations. We used a thermal Green's function model in MATLAB, which considers the response of the device to an impulse of heat generation at one or a series of points. While each Green's function result is only valid for heat generation at a single point, by summation we can

extend the validity of this model to accurately represent the response of an array of particles such as our MPA[38]. Previous work has demonstrated the validity of modeling systems such as ours as a heated disk on a semi-infinite slab, and has further shown that because the thermal conductivity of the substrate (sapphire - 25 W/mK, quartz – 1.3 W/mK) is several orders of magnitude higher than air (0.026 W/mK), we can assume the substrate surface is an adiabatic boundary[40]. For the MPA structure we use periodic, adiabatic boundaries for the unit cell boundaries (perpendicular to antenna plane), while for the lens structure we use open boundaries. By integrating the simulated volumetric loss in each structure, we were able to determine the spatial temperature change for a given intensity of illumination. As the majority of the optical loss occurs in the VO_2 films, this allows us to determine the approximate electrical resistance change of each device, which in turn allows us to determine the sensitivity of our devices. The model predicts a temperature change of 121 K and 232 K in the MPA and plasmonic lens structures respectively, for continuous wave (CW) illumination at an intensity of 7 mW/μm^2 (see Figure 2.5). Thus, to achieve complete switching of VO_2 (approximately 25 K based on our experimental results shown in Figure 2.3a) we would need an illumination intensity of 1.5 mW/μm^2 for the MPA structure, and 0.8 mW/μm^2 for the plasmonic lens structure, based on the assumption of linear scaling of the temperature with illumination intensity. These results are equivalent to a $\frac{\Delta T}{P}$ of $15.0\ {}^{K * \mu m^2}/_{mW}$ for the MPA structure and $31.3\ {}^{K * \mu m^2}/_{mW}$ for the lens structure.

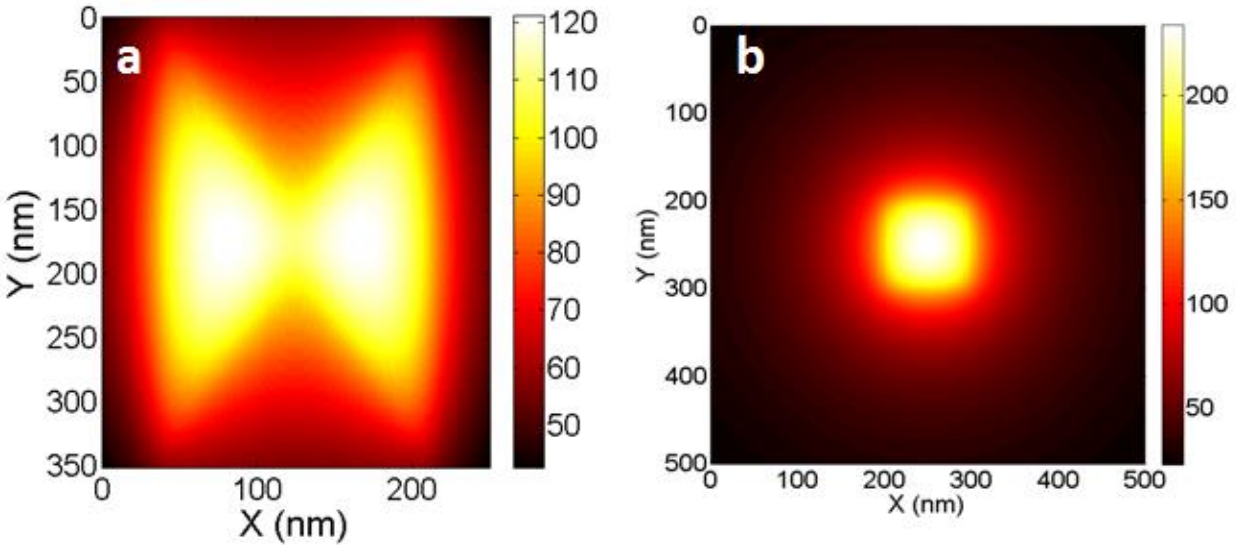

Figure 2.5 – Models of spatial temperature variation in an MPA (a) and plasmonic lens structure (b) under continuous laser illumination at experimentally realizable levels of 7 mW/μm^2. Simulations predict a factor of 2 increase in temperature change in the lens structure over the MPA structure, with both structures experiencing >100 °C temperature increase.

Two common measures of sensitivity for bolometric devices are the noise equivalent temperature (NET) and noise equivalent power (NEP), which indicate how strong of a signal will be distinguishable above the thermal noise background. The theoretical limit of NET and NEP are only functions of device temperature and materials properties. The formula for determining NET is

$$NET = {\Delta R}/{\frac{\partial R}{\partial T}}$$

where ΔR is the minimum detectable resistance change, and $\frac{\partial R}{\partial T}$ is the resistance change as a function of temperature at the transition edge in VO_2. Assuming a minimum detectable resistance of 1 Ω in a 10 kΩ device, this gives a noise equivalent

temperature (NET) of 85 mK, which is at the lower end of the range of reported NET values for uncooled bolometers. The NEP is calculated as

$$NEP = \sqrt{4k_B G_a} T$$

where k_B is Boltzmann's constant, G_a is the thermal conductance of the system, which we approximate as the thermal conductance of the metal leads, T is the operating temperature of the device, which we assume to be 300 K (although operation at the VO_2 transition edge would increase the operating temperature, and thus the noise level). Based on these assumptions[41,42], we estimate an NEP of $9 * 10^{-12}\ {}^{W}/_{\sqrt{Hz}}$.

Using the theoretical NEP, we can determine another measure of sensitivity, the specific detectivity

$$D^* = \frac{\sqrt{Af}}{NEP}$$

where A is the area of a single unit cell (250 nm x 350 nm) and f is the detection bandwidth. Detectivity is generally reported as ${}^{D^*}/_{\sqrt{f}}$, which for our devices is estimated to be $3 * 10^{6}\ {}^{cm\sqrt{Hz}}/_{W}$ [43]. For most bolometers, an absorbed IR photon will produce a signal proportional to the energy of the photon, or about 10^{-19} J. Thus, most uncooled bolometers require a minimum of 100 million photons per second to register an event. NEPs for superconducting detectors are much lower at $\sim 10^{-18}\ {}^{W}/_{\sqrt{Hz}}$, and detectivities much higher at $\sim 10^{11}\ {}^{cm\sqrt{Hz}}/_{W}$ [6,44,45,46,47]. However, our detector is much more sensitive than these sensitivity metrics would imply, because they fail to consider device geometry, particularly the strong enhancement afforded by plasmonic devices.

To achieve a better understanding of the sensitivity of our devices, we will now consider the responsivity, which is given by

$$\Re = \alpha V \frac{\Delta T}{P}$$

where α is the temperature coefficient of resistance (TCR) of VO_2, V is the probe voltage applied to the device, ΔT is the temperature change in VO_2 for incident optical power P[48]. Assuming a probe voltage of 1 V, using reported values for the TCR of VO_2, and the $\frac{\Delta T}{P}$ obtained from our Green's function model, we obtain a responsivity of $1.4 * 10^5 \ {}^{V}/_{W}$. As expected, while our NEP and detectivity values are typical for VO_2 microbolometers, the predicted responsivity is among the highest reported values for uncooled detectors due to the large ratio of temperature increase to incident power afforded by our near perfect absorption and plasmonically enhanced heating[49,50]. Superconducting detectors do still have higher responsivities $(\sim 10^9 \ {}^{V}/_{W})$ [51]. Based on the responsivity, we can calculate an effective NEP which is takes into account our plasmonic enhancement

$$NEP_{eff} = {}^{N_0}/_{\Re},$$

where N_0 is the thermal noise

$$N_0 = \sqrt{4 k_B T R}$$

and R is the device resistance. This gives us an improved value of $3 * 10^{-13} \ {}^{W}/_{\sqrt{Hz}}$, nearly two orders of magnitude higher than the original noise-only value.

In applications such as astronomy and spectroscopy, it is important not only that a detector be highly sensitive, but that it be capable of detecting a wide range of

intensities without saturating. The measure of this capacity is the dynamic range, and is given by

$$DR = 10\ x\ \log_{10}\frac{P_{max}}{P_{min}}\text{, or}$$

$$DR = \log_2\frac{P_{max}}{P_{min}}$$

where P_{max} is the highest detectable power and P_{min} is the lowest detectable power and dynamic range (DR) is given in decibels for the first equation and bits, or stops, for the second. In our device, the lowest detectable power is equivalent to NEP_{eff}, and the highest detectable power can be determined by the power necessary to induce complete switching (25 °C, see Figure 2.3a), which based on our Green's function model is ~1.8 mW, for a dynamic range of 33 bits (98 dB). Common values for microbolometers are in the range of 18 bits (55 dB), approximately four orders of magnitude lower than our value[52,53] while superconducting detectors have ranges which are smaller by a factor of more than 10^6 [54,55]. It is important to note that superconducting detectors rely on crycooling to reduce noise levels, and that they would suffer significant penalties to performance if operated at room temperature like our devices. While we have compared our theoretical values here to experimental values in the literature, our range is still exceptionally large for bolometers due largely to the significantly reduced power of our minimum detectable signal.

One final area where our devices will surpass traditional bolometers is the detection speed, which will be limited by the switching time of VO_2 and the thermal relaxation of the system. VO_2 has been determined to switch in sub-picosecond time scales, with measurements demonstrating switching in as little as 200 fs [56]. Thermal relaxation in our system is modeled by

$$T = T_0 e^{-t/\tau_h}$$

where we can estimate τ_h using a heat flux model

$$\tau_h = R_{BD} C_f t$$

where R_{BD} is the thermal boundary resistance between VO_2 and sapphire, C_f is the volumetric heat capacity, and t is the film thickness[57]. For a film thickness of 50 nm, and using reported values of R_{BD}(0.4*10^{-3} K cm^2/W) and C_f (3.05 J/(cm^3 K)) from the literature[57], we determined a reset time of 6 ns. This time is comparable to the fastest reported reset time for a superconducting detector[58] and at least an order of magnitude faster than typical bolometric devices[59] due to the highly localized plasmonic heating in VO_2.

We have computationally determined the optical, electrical, and thermal properties of our devices, and from this information have determined theoretical limits on the performance we can achieve. Our detector is predicted to have higher responsivity, effective NEP, and speed when compared to bolometers, and higher dynamic range when compared to superconducting detectors. Our devices will maintain the simplicity, portability, and low cost of bolometers, while achieving significantly higher system efficiencies in a thinner active material. In the next chapters we will discuss the fabrication and testing of these devices, and we will compare the experimental results to the theoretical performance.

	Plasmon Enhanced Bolometer	Superconducting Detector	Bolometer
Noise Equivalent Temperature (mK)	85	>10	80-200
Noise Equivalent Power (W/√Hz)	$9*10^{-12}$ ($3*10^{-13}$)	10^{-19}-10^{-18}	10^{-12}-10^{-9}
Specific Detectivity (cm*√Hz/W)	$3*10^{6}$	$<10^{11}$	10^{6}-10^{8}
Responsivity (V/W)	$1.4*10^{5}$	$<10^{9}$	10^{5}-10^{7}
Dynamic Range (bits)	33	<13	14-18
Detection Speed (s)	$6*10^{-9}$	$5*10^{-9}$-10^{-1}	10^{-8}-10^{-1}

Table 2.1 –Comparative summary of performance metrics and figures of merit for the plasmon enhanced bolometers investigated in this study and typical superconducting and bolometric IR detectors.

CHAPTER 3

Metamaterial Perfect Absorbers

3.1 Fabrication

MPA structures were fabricated as shown in Figure 3.1. Five hundred micron thick quartz wafers were cleaned in sequential room temperature baths of acetone, isopropyl alcohol, and water for 1 minute each, and then cleaved into 1 cm^2 pieces. Each piece was coated in 100 nm gold by thermal evaporation. The gold layer was then coated in a thin (<10 nm) insulating dielectric by one of a variety of methods, including atomic layer deposition and electron beam evaporation. A continuous 50 nm VO_2 film was then deposited using electron beam evaporation. These VO_2 films were subsequently annealed for 10 minutes in 250 mTorr oxygen, at a flow rate of 15 sccm, in a quartz tube furnace heated to 450 °C. Films were allowed to cool in the low-pressure oxygen environment for 10 minutes before removal from the furnace. Following the annealing step, the gold was observed in a dark field microscope configuration to confirm that it was not damaged.

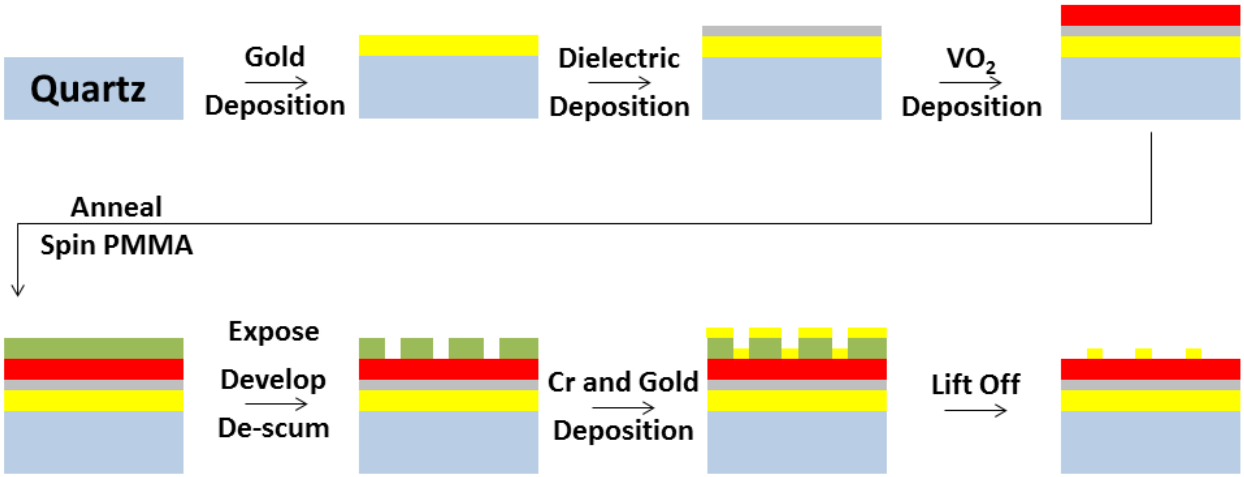

Figure 3.1 – Process diagram for the fabrication of MPA structures. A cleaned quartz wafer is coated in gold, a dielectric barrier, and VO_2. The VO_2 is annealed and coated in PMMA, which is exposed by electron-beam lithography. After development and a de-scum step, the sample is coated in a layer of Cr and gold. The residual PMMA and undesired Cr/gold is removed by a lift off procedure, leaving a functional device with a patterned antenna layer.

Switching of the bulk VO_2 films was confirmed and characterized by measuring the magnitude of transmitted light, or the spectrum of reflected light, for a white light source as the sample was heated from room temperature to 90 °C. Resistivity switching was measured by varying temperature or bias voltage on a resistor structure composed of a 1 x 1 µm or 5 x 5 µm patch of VO_2 deposited across gold electrodes on quartz or sapphire. The stoichiometry of the films was independently confirmed by the presence of characteristic RAMAN peaks at 192 and 222 cm^{-1} [33]. Thickness of the VO_2 films was confirmed by atomic force microscope (AFM) after annealing, as the annealing step can cause changes in both the thickness and surface morphology of VO_2 films. Samples were prepared for electron beam lithography (EBL) by spin coating with A-5 PMMA (5% in anisole) at 4000 rpm for 45 seconds, and subsequent soft baking in air at 180 °C for two minutes. An array of 300 x 400 MPA unit cells (~100 x 100 µm) was patterned onto the substrate by EBL, with alternating rows of antennas connecting to large (200 x 200

μm) bond pads. Samples were developed for 2 minutes in a 3:1 IPA:MIBK solution, which was allowed to thermally equilibrate with an ice water bath for several minutes prior to development. Samples were subsequently rinsed in pure IPA to stop development. Samples were etched in a 120W oxygen plasma for 3 seconds to clean the exposed VO_2 surfaces of any residual developed PMMA. To confirm that the plasma clean did not damage the VO_2, some bare VO_2 samples were etched in an oxygen plasma for several minutes and subsequently characterized as described above. A chromium adhesion layer and gold antenna layer were deposited consecutively by thermal evaporation. Unexposed PMMA was removed by lift-off for at least one hour in a PG remover bath heated to 70 °C. Gold thickness was determined by AFM, and device dimensions were determined by a combination of AFM and SEM characterization. Devices were then mounted onto a ceramic leadless chip carrier (LCC), in which all of the leads were shorted at all times when the device was not undergoing testing, and electrically connected by wire bonding.

3.2 Measurement and Results

Figure 3.2b confirms that our fabricated MPA devices absorbed more than 95% of incident light at 1410 nm, which was slightly blue-shifted from our design wavelength. Thicknesses of both the VO_2 and antenna layers were confirmed by AFM to match the design thicknesses to within 1 nm. However, while the SEM image in Figure 3.2a shows that the realized structure qualitatively matches the design, careful SEM and AFM measurement of device dimensions revealed slight discrepancies which, when included

in the FDTD simulations, provided good agreement with the observed shift of the absorption resonance. Gold maintained good optical quality after VO_2 annealing.

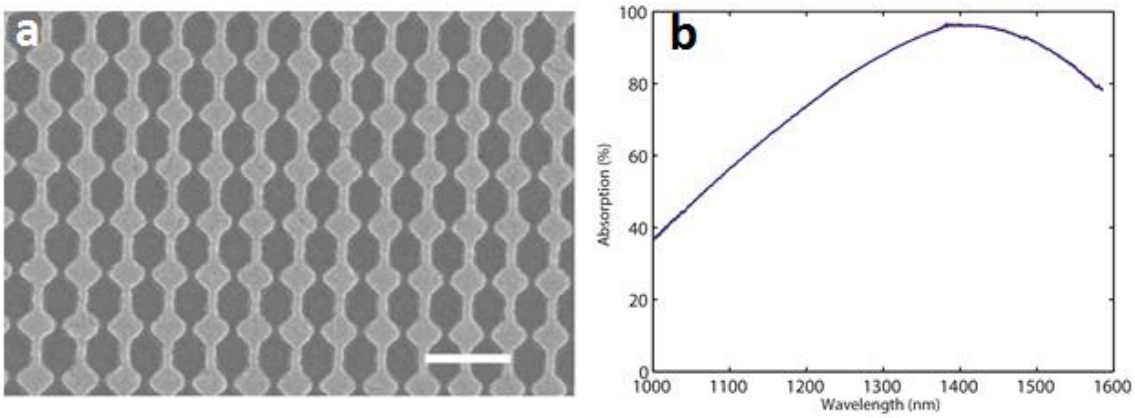

Figure 3.2 – Electron micrograph (a) of an array of bowtie antennas in a metamaterial perfect absorber geometry (scale bar 500 nm). This device achieved greater than 95% absorption of incident light at 1410 nm (b).

Device characterization consisted of both optical and electrical characterization. A schematic of the set up used for optical characterization of the bowtie MPA structure is shown in Figure 3.4. An incandescent mercury white light source was focused through a 20 x objective onto the devices, and both the reflected and transmitted light were coupled through a fiber optic into a spectrometer with a LN2 cooled InGaAs detector. The reflection signal was normalized to a gold mirror, and the transmission (collected by a 50 x objective behind the samples) was normalized to a bare substrate, for two orthogonal linear polarizations.

Electrical measurements showed a resistance much lower than what was expected for a current passing through the arrays. The resistance was determined analytically to correspond to a single pass of the current from the bond pads, through the VO_2, and into the reflective back plane, rather than along the bus bars and through the VO_2 along the gap between the antennas as designed. Upon SEM characterization

of the devices, we determined that the dielectric layer, which was deposited between the VO_2 and the reflective back plane, was not continuous. Figure 3.3 shows a typical film, with isolated, light-colored islands of dielectric with diameter <100 nm, and large, dark-colored regions of exposed gold. This failure of the dielectric film to wet the gold substrate effectively shorted the device at the bond pads, such that we were unable to electrically characterize the MPA structures. After trying various methods of deposition, we determined that atomic layer deposition (ALD) would provide the greatest chance of success due our stringent thickness requirements necessary to maintain optical performance, but we had only limited access to ALD facilities and thus decided to begin investigation of the plasmonic lens geometry.

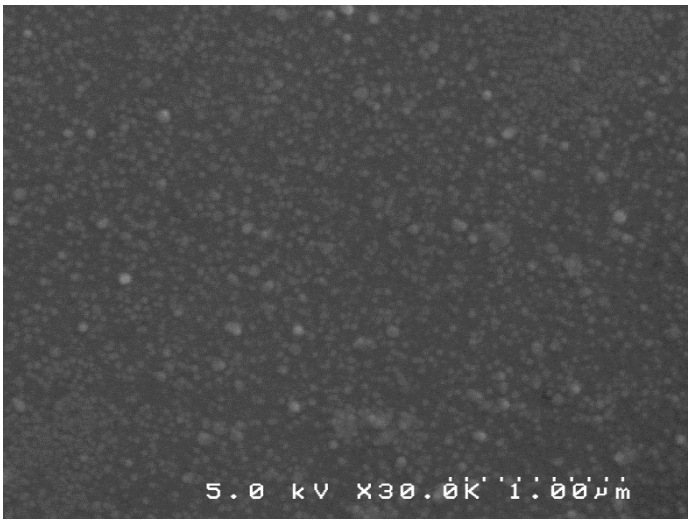

Figure 3.3 – Electron micrograph of 20 nm ALD Al2O3 on gold. The growth of the dielectric layer is still in an island forming regime, which results in a discontinuous and ineffective dielectric barrier.

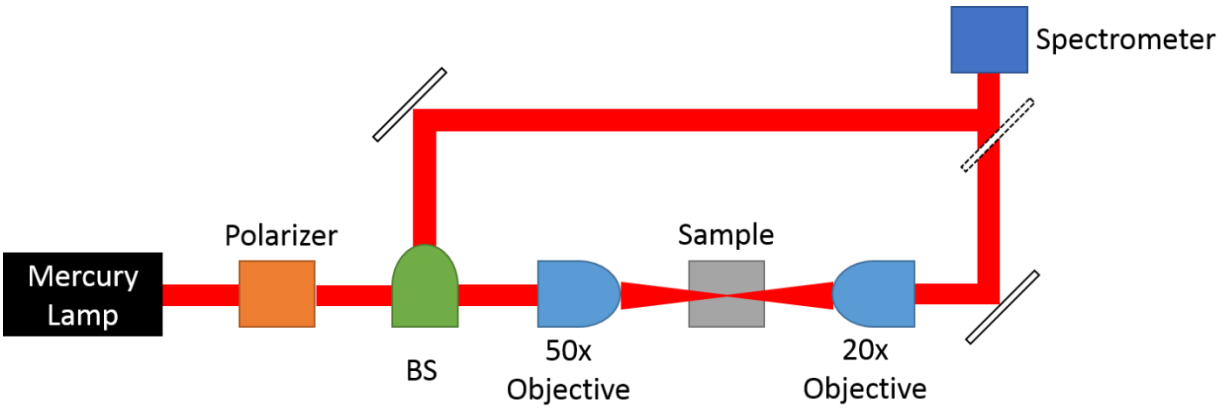

Figure 3.4 – Optical set up used for characterization of absorption in the MPA structure. A polarized mercury white light source is focused incident on a sample, and the use of a beam splitter (BS) in conjunction with a switchable mirror allows collection of either the reflected or transmitted signal.

CHAPTER 4

Plasmonic Lenses

4.1 – Fabrication and VO_2 Etching

Plasmonic lens structures were fabricated as shown in Figure 4.1, starting with cleaned quartz or double polished c-cut sapphire wafers. The lattice constant of sapphire has been shown to be similar enough to VO_2 to allow for epitaxial growth[60]. All wafers were patterned with a square lattice of cross-shaped chrome alignment markers at 200 µm spacings by standard photolithography, thermal evaporation, and lift off in PG remover, to facilitate subsequent EBL processing.

Following deposition of the alignment markers, the VO_2 patches were defined by either a lift off method or plasma etching. The lift off method consisted of EBL patterned deposition of VO_2 onto the sapphire substrate. This method requires the VO_2 annealing time to be reduced from 10 minutes to 4 minutes to prevent the nanoscale VO_2 patches from entering a higher oxidation state which does not show switching behavior. In the plasma etching method, a bulk VO_2 film was deposited and annealed normally, and EBL was subsequently used to define the areas where VO_2 is desired. A gold mask was deposited on top of these areas by thermal evaporation, and after lift off the unmasked VO_2 was removed by plasma etching. The etch recipe is a modified form of a recipe described by Ramanathan[61] and consists of 12 seconds etching at 50 mTorr in a 100 W ICP/50 W RIE plasma, with 10 sccm O_2 and 10 sccm CF_4. The gold mask was subsequently removed by chemical etching in a TFA-type etchant. After the VO_2 layer

was defined and annealed, the gold antenna layer was defined by EBL and deposited by thermal evaporation. Once lift off was completed, devices were wire bonded to prepare the devices for electrical characterization.

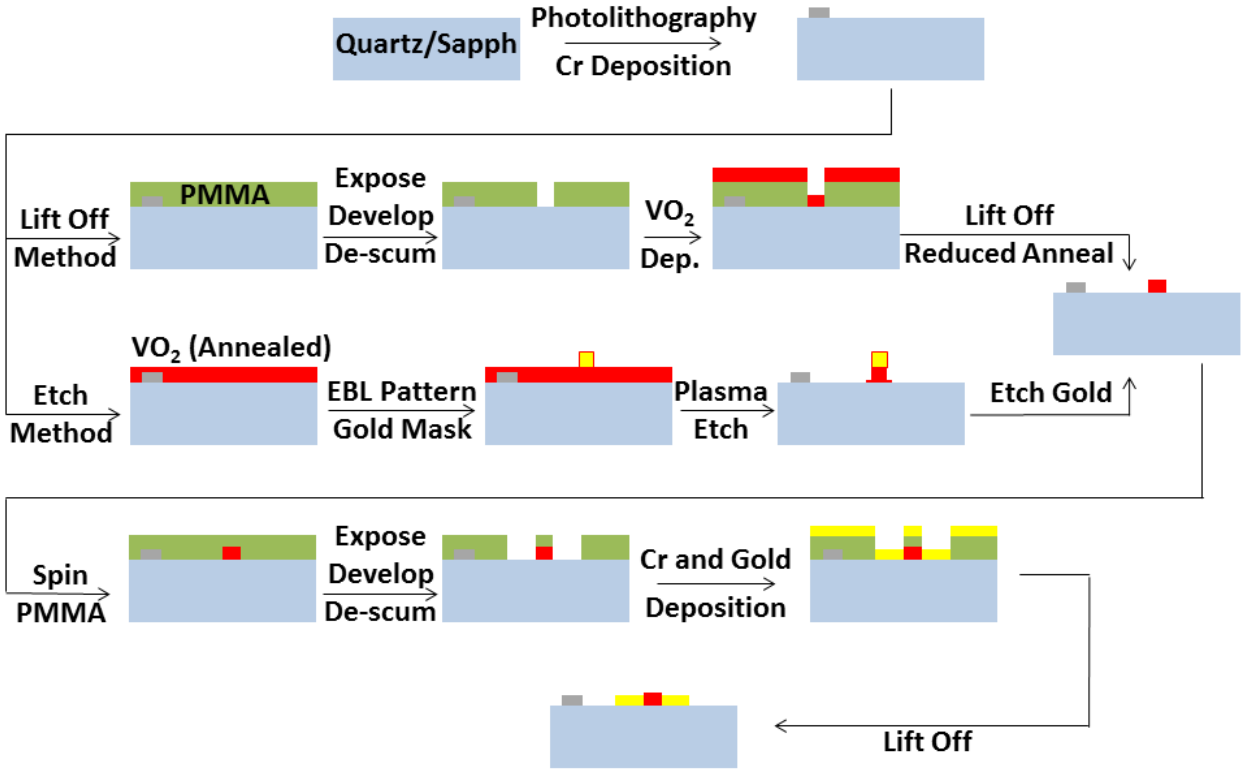

Figure 4.1 – Process diagram for the fabrication of plasmonic lens structures. A cleaned quartz or sapphire wafer is coated in alignment layers to allow for multi-layer EBL patterning. Nanoscale VO_2 features are then defined by either a lift-off method or an etch method. The lift off method consists of direct EBL patterning of VO_2, which for properly reduced annealing times produces a higher quality film. The etch method consists of depositing and annealing a bulk VO_2 thin film, followed by depositing an EBL patterned gold etch mask, plasma etching, and chemical etching to remove the gold mask. This method allows for more straightforward achievement of correct stoichiometry, but leaves shelf-like deposits of lattice-matched VO_2 which reduce the quality of subsequent layers. Once the VO_2 has been defined and deposited, the gold antenna layer is patterned by EBL and deposited by thermal evaporation.

4.2 – Results

Plasmonic lenses were initially fabricated on quartz substrates, using a plasma etch process to define VO_2 dimensions. Electrically connected plasmonic lens devices were heated to determine the magnitude of resistance change in the small VO_2 patches. While the order of magnitude of resistance of these devices at room temperature corresponded well to analytical predictions, the resistance change for small VO_2 patches was consistently less than two orders of magnitude, compared to the ~3 orders of magnitude which is observed in bulk films. Our initial concern was that the small patches were a non-stoichiometric oxide of vanadium. Figure 4.2d shows data from a typical confocal RAMAN scan of the fabricated patches, where the presence of strong peaks at 192 and 22 cm^{-1} confirms the presence, and prevalence, of the correct stoichiometry. Having demonstrated that our switching material was stoichiometric VO_2, we fabricated various sized patches for electrical testing to attempt to determine a size dependence of the switching. When no direct relation between particle size and switching magnitude was observed, we decided to switch to sapphire substrates to increase the crystallinity and grain size of the VO_2, and to increase the stability of the annealed oxide.

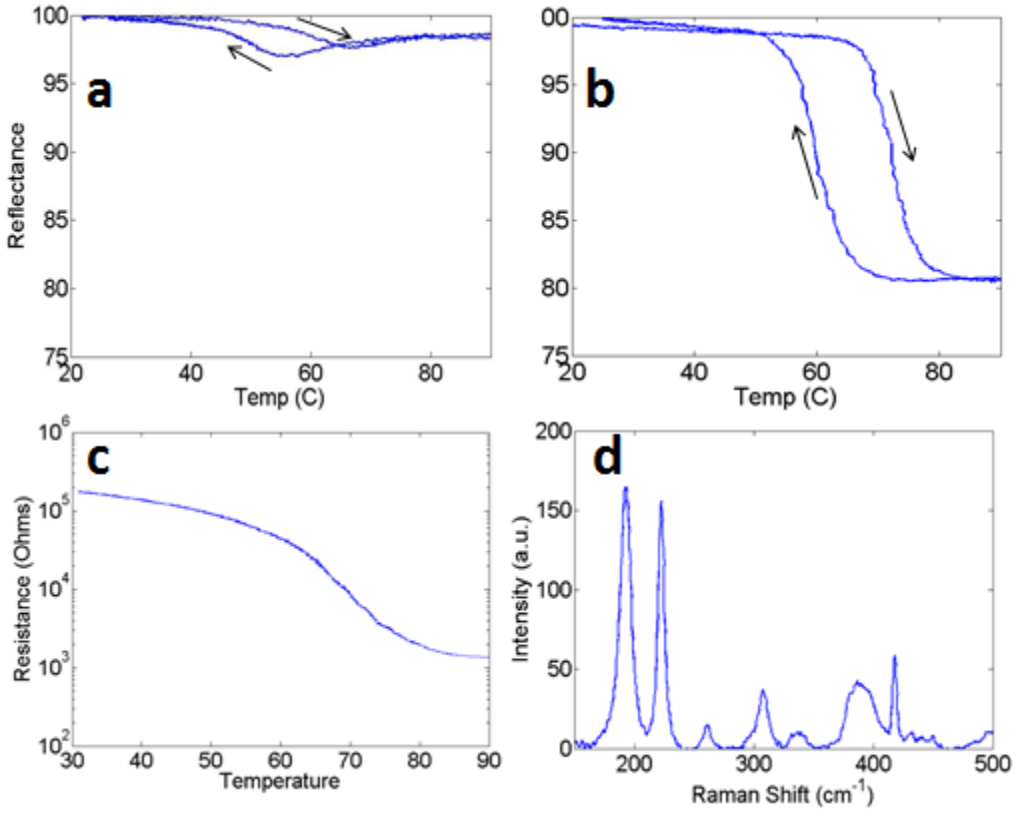

Figure 4.2 – Switching magnitude of VO_2 on quartz (a) and sapphire (b). The magnitude of switching is greatly enhanced on sapphire due to lattice matching at the surface.[33] The change in electrical resistance of a nanoscale patch of VO_2 on sapphire fabricated by a lift off method is ~2 orders of magnitude (c), which while large relative to many materials is still significantly less than what is observed in bulk films. The stoichiometry of these films was verified by the presence of a strong RAMAN signal at 192 and 222 cm^{-1} (d).

As expected, the increased crystallinity of the VO_2 on sapphire substrates resulted in increased repeatability and magnitude of switching, as seen in the reflectance data in Figure 4.2a-b. The EBL patterning of the antenna layer translated well to sapphire substrates, but when VO_2 was etched on sapphire, a number of problems arose. For etch times comparable to what was used on quartz, a significant amount of undesired residual VO_2 was left on the substrate. These plasma roughened patches scattered light strongly, and affected the surface morphology and electrical

performance of subsequent device layers. When etch times were increased to remove all undesired VO_2, there was a large (up to 1 μm) shelf around each patterned feature on which the VO_2 was overetched to a thickness of ~10 nm, regardless of the original thickness of the bulk thin film. This shelf can be observed in Figure 4.3, where the high crystallinity of the VO_2 is apparent as a series of star-shaped patterns on the surface of the unetched material. It was determined that there are two etch rates for VO_2 on sapphire, due to the first ~10 nm above the sapphire, which is lattice matched and strained, etching at a slower rate than the remainder of the film. While subsequent process engineering enabled us to reduce the shelf widths to <100 nm, and still remove all undesired VO_2, this width is comparable to the desired dimensions of our VO_2 patches. We thus switched to a lift-off based method, which allowed much higher fidelity definition of VO_2 patches.

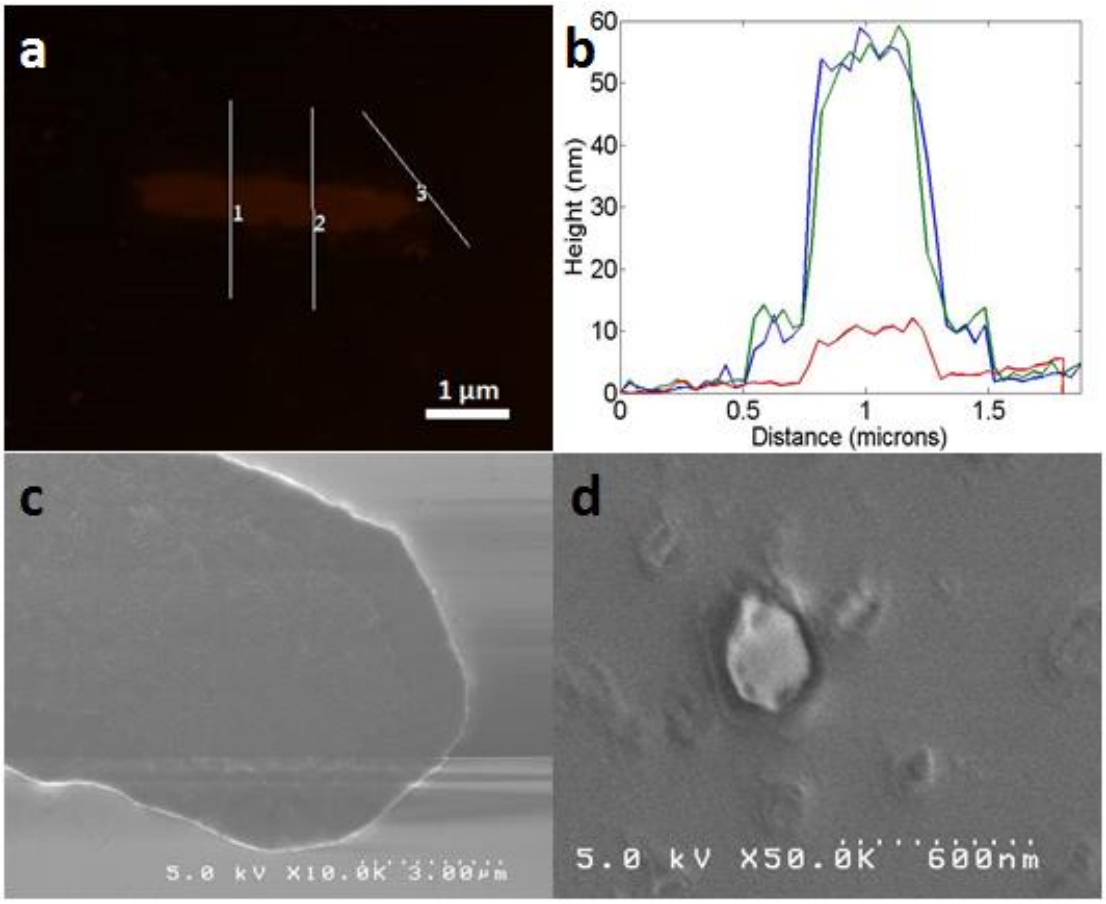

Figure 4.3 – AFM (a) and SEM (c) scan of VO_2 features on sapphire, defined by plasma etching. The AFM line profiles (b) show two distinct levels of the VO_2, suggesting different etch rates for the initial epitaxial growth and the subsequent unstrained VO_2. Etch process engineering can reduce the etch rate differences such that the epitaxial "shelf" extends for less than 100 nm (d) beyond the edge of the defined feature, but as this is comparable to the overall dimension of the simulated VO_2 patch, a lift-off method was pursued instead.

While the switch to a lift off method was necessary to allow for accurate definition of the VO_2 patches, it added increased difficulty by forcing us to anneal the VO_2 in nanoscale patches rather than as a bulk thin film. To achieve the correct stoichiometry, we thus needed to decrease the annealing time according to the size of patch we were attempting to obtain. For patch sizes of 100 nm, we found that an annealing time of 4 minutes at 450 ˚C produced the strongest switching. Failure to properly tune the

annealing step resulted in the formation of a non-stoichiometric film with weak or no switching, but even optimized annealing of nanoscale VO_2 resulted in weaker switching than in bulk films. We believe that this reduction in switching magnitude, which reduces the experimentally realizable sensitivity of our devices, is due to the fact that as the size of the patches approaches the size of the VO_2 grains, the effect of individual defects or stoichiometric variations can no longer be statistically averaged out from the response of the patch.

Figure 4.4b shows an array of 100 nm square patches of VO_2 on sapphire. These squares were defined by a lift-off method, and have high fidelity to the design dimensions with no shelf-type residue remaining. RAMAN measurements have shown these films to be stoichiometric. Figure 4.4a further confirms the fabrication of plasmonic lenses in accordance with our design. These devices were electrically characterized as described in the next chapter.

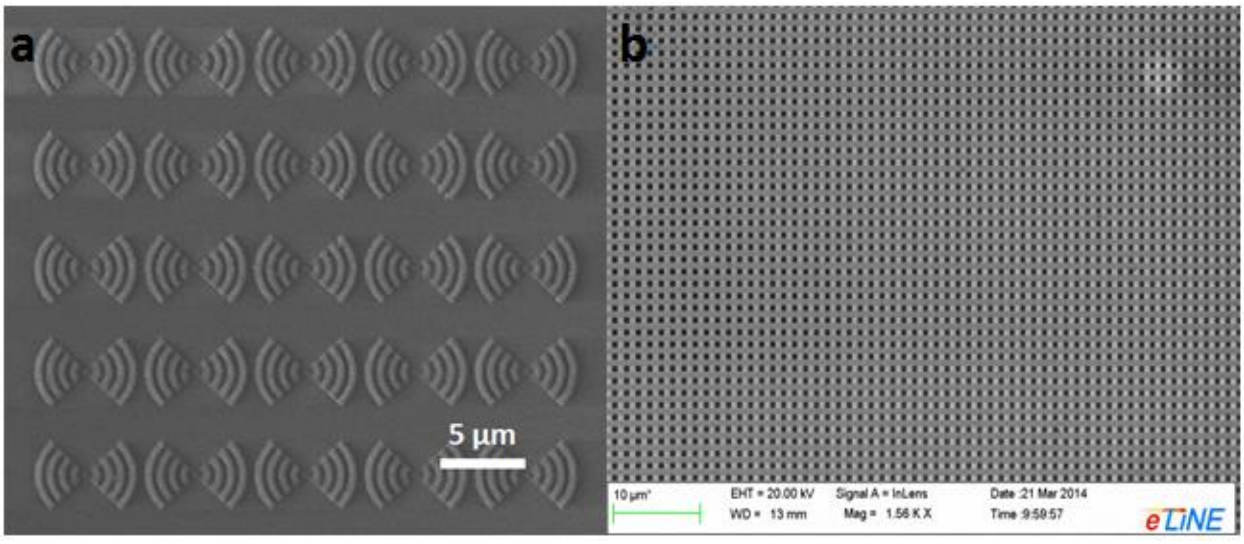

Figure 4.4 – Electron micrographs of an array of plasmonic lens structures (a) and 100 nm square VO_2 patches on sapphire defined by a lift off method (b). Both structures show good fidelity to the design.

CHAPTER 5

Electrical Characterization

Having developed a method for realizing the plasmonic lens structure, we turned to electrically characterizing the performance of the devices. It was found that the devices, each of which funneled current through a single 100 nm square patch of VO_2, were highly sensitive to electrostatic discharge (ESD). Thus for initial device performance characterization we used the 1 μm resistor devices, which had been designed to simplify characterization of the VO_2 switching.

Electrical characterization was accomplished by connecting the samples to a Keithley 2400 source meter, which output data at a rate of 10 Hz to a computer. During electrical testing, samples were placed in the beam path of either a 405 nm diode laser or a 1550 Ti:Sapphire laser, each of which were focused through a 20 x objective onto the devices. Laser power was measured by a power meter, and the intensity was attenuated by inclusion of optical density filters and linear polarizers. For some samples, an optical chopper was placed in the beam path and the current through the device was fed through a SR-830 Lock-In Amplifier. Temperature of the devices was controlled either locally by the magnitude of the applied voltage or across the sample by use of a resistive heater.

These devices were electrically biased with a small voltage (0.1 V), and subsequently illuminated by CW laser light at 405 nm or 1500 nm. The laser light was focused through a 20x objective such that only the patch of VO_2 was illuminated. A

detection event was defined as any instantaneous resistance change detectable above the noise background. Initial tests with high laser powers (1 W) resulted in strong switching, albeit with a marked latching of the resistance state. The “latched” low resistance state was found to slowly return to the initial high resistance state over a period of several minutes. Turning off the bias voltage did not increase the speed of reset. Reducing the laser power reduced the magnitude of observed switching, but not the presence of latching behavior. A series of experiments was conducted in which the duration and power of illumination were varied. The results of these experiments can be seen in Figure 5.1, where we found that with increasing illumination time and power, the percent of overall change in resistance which “latched” increased. This indicated heating of the substrate in an area much larger than the VO_2 patch.

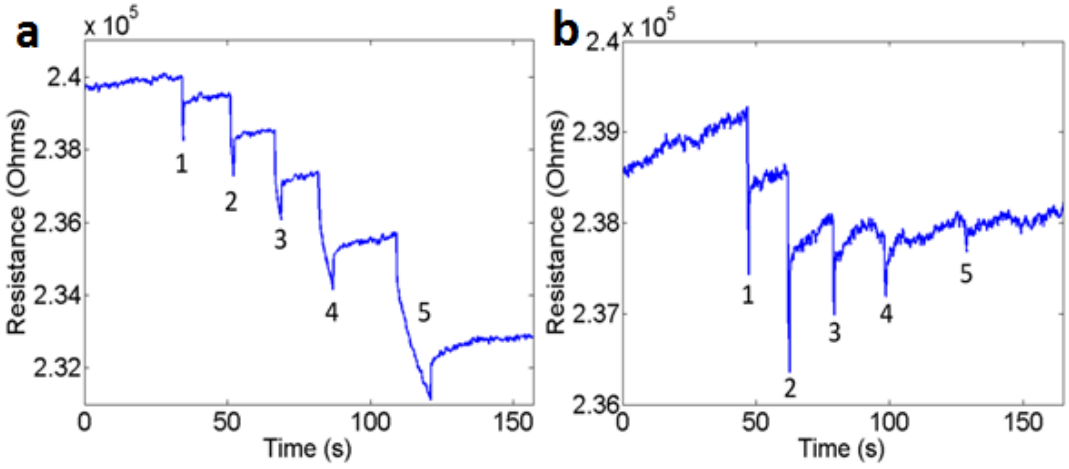

Figure 5.1 – Electrical response of a 1 µm VO_2 resistor to increasing duration of laser illumination (a) at 405 nm. From left to right, the numbered peaks correspond to illumination for: 0.5 s, 1 s, 2 s, 5 s, and 10 s. Note that with increasing duration of illumination, there is a greater amount of residual decrease in resistance, indicating a residual increase in temperature. Electrical response of a 1 µm VO_2 resistor to decreasing intensity of laser illumination (b). From left to right, the numbered peaks correspond to illumination at a power of: 150 mW, 200 mW, 100 mW, 50 mW, and 25 mW. Note that with increasing power, there is indication of residual heating, which would suggest that even at low powers and short illumination times, the surrounding substrate is significantly heated.

Because of the de-localized substrate heating and high noise levels, our sensitivity at 405 nm was limited to ~20 mW. Changing the wavelength from 405 nm to 1550 nm decreased absorption in the device overall, but more especially in the metal and substrate such that detection events did not result in latching behavior or slow recovery times. In addition to this improvement in reset speed, an improved focusing set up allowed us to increase our sensitivity by an order of magnitude to ~1 mW as seen in Figure 5.2a. While this increase in realizable sensitivity was large, it still left us several orders of magnitude below the theoretical sensitivity of even the simple resistor device. As the sensitivity is defined by both the response to a signal, which for the resistor was a function of known and fixed materials properties, and the noise level of the device, we decided to characterize the noise level of our resistors. Data was collected on 1 μm resistor devices under ambient conditions. At a realistic probe voltage of 0.75 V, a typical device such as the one tested in Figure 5.3a produced an average noise level 1%. For comparison, additional data is provided in Figure 5.3b which was taken on a commercial carbon film resistor of approximately equivalent resistance, which had a noise variance of <0.001% at the same temperature and measurement frequency. The noise level in the VO_2 resistors was further observed to decrease as a function of voltage, which indicates a significant shot noise contribution due to the small cross section, and correspondingly small current, of our devices. This significant noise level in the VO_2 device is able almost exclusively to account for the difference between theoretical and experimental sensitivity. While a single photon detector would be unable to incorporate signal averaging or other common noise reduction methods, we decided to construct a set up with a lock-in amplifier in order to further check the accuracy our

model, which incorrectly assumed a low-noise environment. Figure 5.2b shows that by using an optical chopper and a lock-in, we were able to detect a signal of 2 μW.

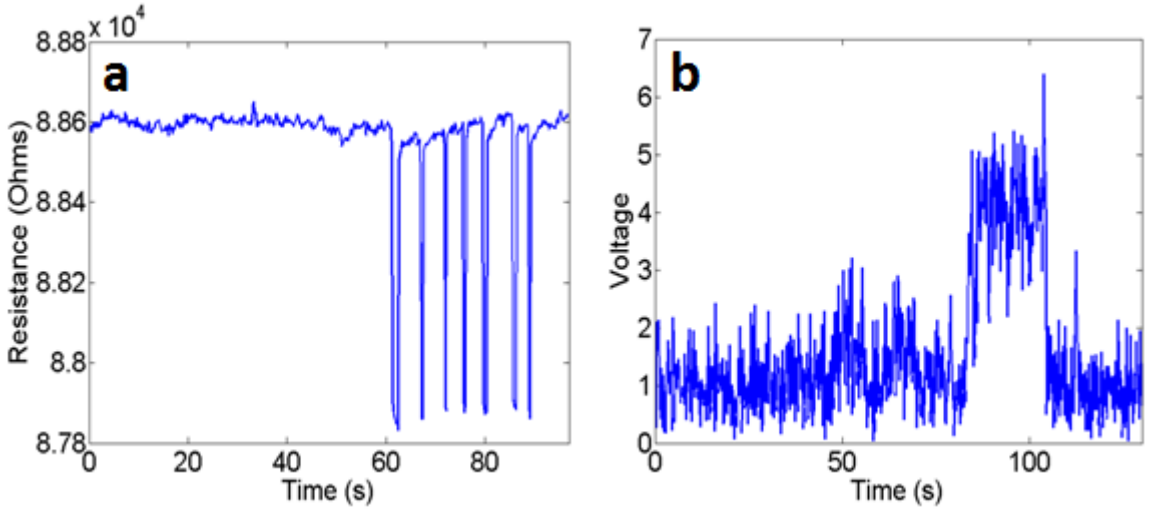

Figure 5.2 – Electrical response of a 1 μm VO_2 resistor to laser illumination at 1550 nm. In a standard configuration, the system responds strongly to 40 mW illumination (a), suggesting a maximum sensitivity of 1 mW. With the addition of an optical chopper and a lock-in amplifier, the sensitivity level can be increased to 2 μW (b). Illumination with an IR laser eliminates the latching behavior seen at shorter wavelengths by reducing absorption in the metal and substrate, such that heat is localized in the VO_2 and dissipates quickly after illumination is stopped.

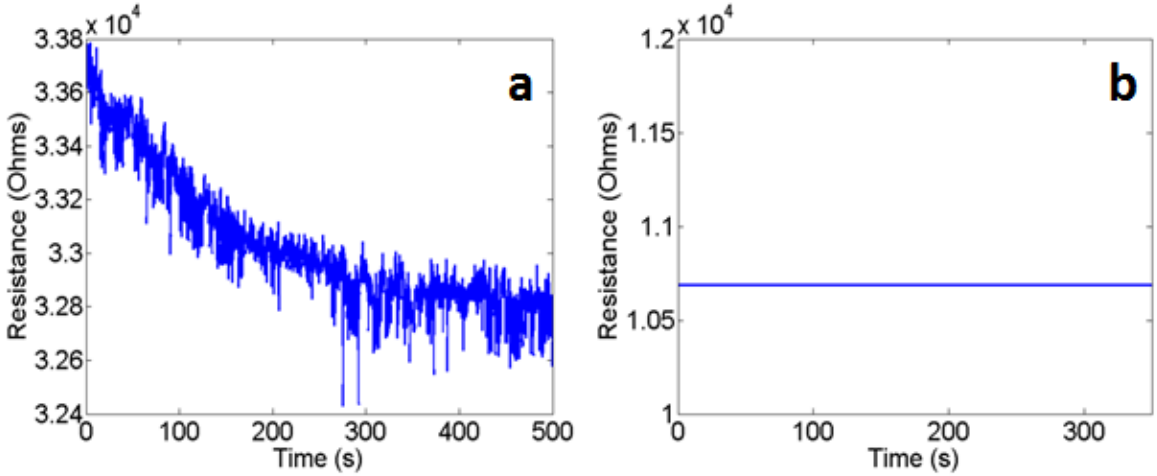

Figure 5.3 – Resistance noise levels for a 1 μm VO_2 resistor (a), and a commercial 10 kOhm resistor (b). The noise in the VO_2 system is several orders of magnitude higher, likely due to shot noise effects, and the signal drifts over time due to temperature changes in the room (this data collected after building air conditioning was shut off). Both of these effects combine to reduce the sensitivity of the device well below the theoretical sensitivity.

CHAPTER 6

Conclusions and Future Directions

In this work we have designed two plasmonic IR photodetectors which combine the room temperature operation of bolometers and the high sensitivities of superconducting detectors or APDs. While in this work we were not able to characterize the electrical performance of a plasmonic IR photodetector, we have fabricated optically active versions of both structures. Through characterization of these structures, we have confirmed the validity of our optical model through the demonstration of high absorption and localized heating. Further agreement between the predicted and realized optical properties can be achieved through improved control over the dimensions of the structure.

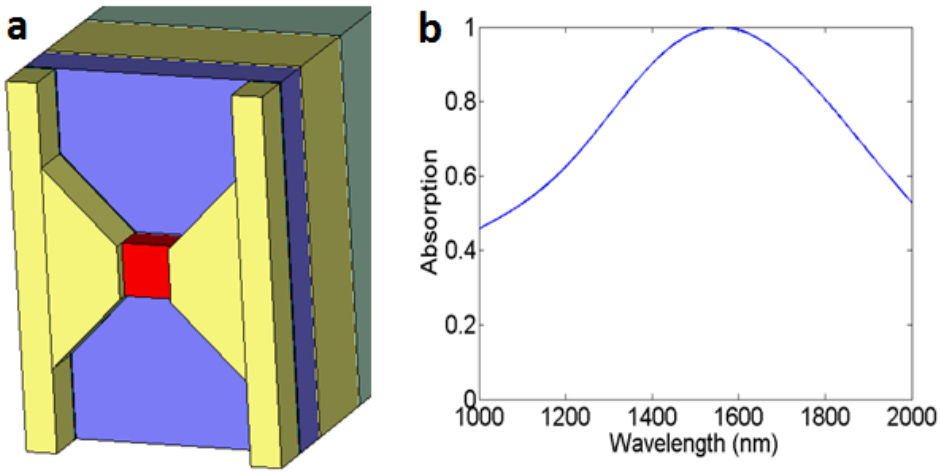

Figure 6.1 – Bowtie MPA design with patterned VO_2 patches (left), which avoids the need for process engineering of a thin dielectric layer on gold. The device has a 30 nm thick layer of Al_2O_3 between the reflective back plane and the antenna layer. The critical dimensions are an antenna gap of 50 nm, bus bar width 45 nm, unit cell dimensions of

250 nm x 350 nm, and a VO_2 thickness of 35 nm. This device achieves a maximum absorption of 99.99% at 1550 nm (right).

Electrical functionality remains to be experimentally verified in future work. If noise in these devices can be mitigated, analytical calculations predict sensitivity to as few as 10 incident photons, which is comparable to or better than the performance of many superconducting detectors. One route to reducing noise may be through placing a large number of devices in parallel, such as in the MPA device. This may be achieved through engineering the deposition process for the dielectric layer, or through the use of patterned VO_2 layer. To facilitate future investigations, we designed the MPA shown in Figure 6.1a, which has patterned VO_2. This device retains a theoretical absorptivity of 99.99% (see Figure 6.1b), and a theoretical sensitivity comparable to our original MPA design. In the course of designing and fabricating these photodetectors, we also developed two methods for fabricating stoichiometric nanoscale VO_2 patches, which may allow further investigation into the dynamics of correlated electron materials.

REFERENCES

[1] J Federici, B Schulkin, F Huang, D Gary, R Barat, F Oliveira, and D Zimdars, “THz imaging and sensing for security applications—explosives, weapons and drugs”, Semicond. Sci. Technol. 20, 2005

[2] RH Hadfield, “Single-photon detectors for optical quantum information applications”, Nature Photonics 3, 2009

[3] PL Richards, “Bolometers for infrared and millimeter waves”, Journal of Applied Physics 76(1), 1994

[4] B Cabrera, RM Clarke, P Colling, AJ Miller, S Nam, and RW Romani, “Detection of single infrared, optical, and ultraviolet photons using superconducting transition edge sensors”, Appl. Phys. Lett. 73, 1998

[5] S Komiyama, “Single-Photon Detectors in the Terahertz Range”, IEEE Journal of Selected Topics in Quantum Electronics 17(1), 2011

[6] F Marsili, VB Verma, JA Stern, S Harrington, AE Lita, T Gerrits, I Vayshenker, B Baek, MD Shaw, RP Mirin and SW Nam, “Detecting single infrared photons with 93% system efficiency”, Nature Photonics 7, 2013

[7] M Csete, Á Sipos, A Szalai, F Najafi, G Szabó, and KK Berggren, “Improvement of infrared single-photon detectors absorptance by integrated plasmonic structures”, Nature Scientific Reports 3, 2013

[8] M Macdougal, J Geske, C Wang, and D Follman, “Short-wavelength infrared imaging using low dark current InGaAs detector arrays and vertical-cavity surface-emitting laser illuminators”, Opt. Eng. 50(6), 2011

[9] A Rogalski, “Infrared detectors: an overview”, IR Phys. Tech. 43, 2002

[10] F Capasso, WT Tsang, AL Hutchinson, and GF Williams, “Enhancement of electron impact ionization in a superlattice: A new avalanche photodiode with a large ionization rate ratio”, Appl. Phys. Lett. 40(1), 1982

[11] E Pomarico, B. Sanguinetti, R Thew, and H Zbinden, “Room temperature photon number resolving detector for infrared wavelengths”, Optics Express 18(10), 2010

[12] SH Lee, KH Jeong, KH Kim, MH Lee, JT Ahn, SH Choi, CW Park, JB Park, and S Moon, “Low-Noise Single-Photon Detector for the 1.5-μm Wavelength Region”, J. Korean Phys. Soc. 50(1), 2007

[13] S Charbonneau, L Allard, J Young, G Dyck, and B Kyle, “Two-dimensional time-resolved imaging with 100-ps resolution using a resistive anode photomultiplier tube”, Rev. Sci. Instrum. 63, 1992

[14] JS Dam, P Tidemand-Lichtenberg, and C Pedersen, “Room-temperature mid-infrared single-photon spectral imaging”, Nature Photonics 6, 2012

[15] L Vicarelli, “Graphene field-effect transistors as room-temperature terahertz detectors”, Nature Materials 11, 2012

[16] JA Schuller, ES Barnard, W Cai, YC Jun, YS White, and ML Brongersma, “Plasmonics for extreme light concentration and manipulation”, Nature Materials 9, 2010

[17] AP Hibbins, “Grating Coupling of Surface Plasmon Polaritons at Visible and Microwave Frequencies”, University of Exeter, 2000

[18] H Raether, “Surface Plasmons on Smooth and Rough Surfaces and on Gratings”, Springer Tracts in Modern Physics, Vol. 111, Springer Berlin 1988

[19] SA Maier, “Plasmonics: Fundamentals and Applications”, Springer, 2007

[20] DJ Barber, and IC Freestone, “An investigation of the origin of the colour of the Lycurgus Cup by analytical transmission electron microscopy”, Archaeometry 32 (1), 1990

[21] PR West, S Ishii, GV Naik, NK Emani, VM Shalaev, and A Boltasseva, “Searching for better plasmonic materials”, Laser Photonics Rev. 4(6), 2010

[22] J Valentine, S Zhang, T Zentgraf, E Ulin-Avila, DA Genov, G Bartal, and X Zhang, “Three-dimensional optical metamaterial with a negative refractive index”, Nature 455, 2008

[23] D Schurig, JJ Mock, BJ Justice, SA Cummer, JB Pendry, AF Starr, and DR Smith, “Metamaterial Electromagnetic Cloak at Microwave Frequencies”, Science 314(5801), 2006

[24] NI Landy, S Sajuyigbe, JJ Mock, DR Smith, and WJ Padilla, “Perfect metamaterial absorber”, Phys. Rev. Lett. 100, 2008

[25] A Sundaramurthy, PJ Schuck, NR Conley, DP Fromm, GS Kino, and WE Moerner, “Toward Nanometer-Scale Optical Photolithography: Utilizing the Near-Field of Bowtie Optical Nanoantennas”, Nano Lett. 6 (3), 2006

[26] Z Liu, JM Steele, W Srituravanich, Y Pikus, C Sun, and X Zhang., “Focusing Surface Plasmons with a Plasmonic Lens”, Nano Lett. 5(9), 2005

[27] W Zhong, Y Wang, R He, and X Zhou, “Investigation of plasmonics resonance infrared bowtie metal antenna”, Appl. Phys. B 105, 2011

[28] C Wen-Jun, L Bin-Hong, and X Tao, “A resonant frequency formula of bow-tie antenna and its application”, Antennas and Propagation Society International Symposium Proceedings, 2004

[29] X Jiao and S Blair, “Polarization Multiplexed Optical Bullseye Antennas”, Plasmonics 7(1), 2012

[30] H Jerominak, D Vincent, and F Picard, “Vanadium oxide films for optical switching and detection”, Optical Engineering 32(9), 1993

[31] A Zylbersztejn and NF Mott, “Metal-insulator transition in vanadium dioxide”, Phys. Rev. B 11, 1975

[32] H Coy, R Cabrera, N Sepúlveda, and FE Fernández. "Optoelectronic and all-optical multiple memory states in vanadium dioxide." J. of App. Phys. 108 (11), 2010

[33] TD Manning, "APCVD of thermochromic vanadium dioxide thin films—solid solutions $V_{2-x}M_2O_2$ (M = Mo, Nb) or composites VO_2:SnO_2", J. Mater. Chem. 15, 2005

[34] RM Briggs, IM Pryce, and HA Atwater. "Compact silicon photonic waveguide modulator based on the vanadium dioxide metal-insulator phase transition." Opt. Express 18 (11), 2010

[35] SH Bae, S Lee, H Koo, L Lin, BH Jo, C Park, and ZL Wang, “The memristive properties of a single VO2 nanowire with switching controlled by self-heating”, Adv Mater. 25 (36), 2013

[36] TD Manning, IP Parkin, ME Pemble, D Sheel, and D Vernardou, “Intelligent Window Coatings: Atmospheric Pressure Chemical Vapor Deposition of Tungsten-Doped Vanadium Dioxide”, Chem. Mater. 16 (4), 2004

[37] S Lee and K Lynch, “Telecommunications Industry Revenues: 2009”, 2011

[38] G. Baffou, R Quidant, and C Girard, “Thermoplasmonics modeling: A Green’s function approach”, Phys. Rev. B 82, 2010

[39] Z Coppens, W Li, DG Walker, and JG Valentine, "Probing and Controlling Photothermal Heat Generation in Plasmonic Nanostructures", Nano Lett. 13(3), 2013

[40] G Baffou, R Quidant, and C Girard, “Heat generation in plasmonic nanostructures: Influence of morphology”, Appl. Phys. Lett. 94, 2009

[41] A Rahman, “Room Temperature Micromachined Microbolometers for W-Band (75 GHz - 110 GHz) Focal Plane Imaging Array”, Massachusetts Institute of Technology, 1996

[42] A Rahman, GD Lange, and Q Hu, “Micromachined room-temperature microbolometers for millimeter-wave detection”, App. Phys. Lett 68(14), 1996

[43] W Song and JJ Talghader, “Design and characterization of adaptive microbolometers”, J. Micromech. Microeng. 16, 2006

[44] AD Beyer, PM Echternach, ME Kenyon, MC Runyan, B Bumble, CM Bradford, JJ Bock, and WA Holmes, “Effect of Mo/Cu Superconducting Bilayer Geometry on Ultra-Sensitive Transition-Edge Sensor Performance”, IEEE T. Appl. Supercon. 23(3), 2013

[45] JT Skidmore, J Gildemeister, AT Lee, MJ Myers, and PL Richards, “Superconducting bolometer for far-infrared Fourier transform spectroscopy”, Appl. Phys. Lett. 82(469), 2003

[46] BG Ghamsari, “Guided-Wave Superconducting Quantum Optoelectronic Devices”, University of Ottowa, 2010

[47] F Marsili, F Najafi, E Dauler, F Bellei, X Hu, M Csete, RJ Molnar, and KK Berggren, “Single-Photon Detectors Based on Ultranarrow Superconducting Nanowires”, Nano Lett. 11(5), 2011

[48] M Nishikawa, T Nakajima, T Manabe, T Okutani, and T Tsuchiya, “High temperature coefficients of resistance of VO_2 films grown by excimer-laser-assisted metal organic deposition process for bolometer application”, Mater. Lett. 64(17), 2010

[49] J. Oden, J Meilhan, J Lalanne-Dera, JF Roux, F Garet, JL Coutaz, and F Simoens, “Imaging of broadband terahertz beams using an array of antenna-coupled microbolometers operating at room temperature”, Optics Express 21(4), 2013

[50] G Fernandes et al., “Carbon nanotube microbolometers on suspended silicon nitride via vertical fabrication procedure”, Appl. Phys. Lett. 104, 2014

[51] AN Vistavkin, JH Kim, M Chin, N Dhar, and J Xu, “Comparison of Two Types of Andreev Reflection Hot-Electron Microbolometer for Submillimeter Radio Astronomy”, Proc. of the 11th Internat. Symp. on Space THZ Tech., 2000

[52] D Svard, C Jansson, and A Alvandpour, “A readout IC for an uncooled microbolometer infrared FPA with on-chip self-heating compensation in 0.35 lm CMOS”, Analog Integr Circ Sig Process 77, 2013

[53] N Liu, Q Chen, GH Gu, and XB Sui, “Microbolometer Dynamic Range Adaptive Technology Based on the Scene Target Temperature Calculation”, Opt. Rev. 18(6), 2011

[54] J Hu, Q Zhao, X Zhang, L Zhang, X Zhao, L Kang, and P Wu, “Photon-Counting Optical Time-Domain Reflectometry Using a Superconducting Nanowire Single-Photon Detector”, J. Light. Tech. 30(16), 2012

[55] MP Croce, MK Bacrania, EM Bond, DE Dry, AL Klingensmith, WA Moody, SP Lamont, MW Rabin, JH Rim, JA Beall, DA Bennett, V Kotsubo, RD Horansky, GC Hilton, D Schmidt, JN Ullom, and R Cantor, “Superconducting Transition-Edge Sensor Microcalorimeters for Ultra-High Resolution Alpha-Particle Spectrometry”, Appl. Supercond. 21(3), 2011)

[56] A Cavalleri, CS Tóth, CW Siders, JA Squier, F Ráksi, P Forget, and JC Kieffer, “Femtosecond Structural Dynamics in VO_2 during an Ultrafast Solid-Solid Phase Transition”, Phys. Rev. Lett. 87(23), 2001

[57] S. Lyenko, A Rúa, V Vikhnin, F Fernández, and H Liu, “Insulator-to-metal phase transition and recovery processes in VO_2 thin films after femtosecond laser excitation”, Phys. Rev. B 76, 2007

[58] X Hu, EA Dauler, RJ Molnar, and KK Berggren, “Superconducting nanowire single-photon detectors integrated with optical nano-antennae”, Opt. Exp. 19(1), 2011

[59] L Mandal, M Deo, A Yengantiwar, A Banpurkar, J Jog, and S Ogale, “A Quasi-Liquid Iontronic–Electronic Light-Harvesting Hybrid Photodetector with Giant Response”, Adv. Mat. 24(27), 2012

[60] TH Yang, R Aggarwal, A Gupta, H Zhou, RJ Narayan, and J Narayan, “Semiconductor-metal transition characteristics of VO_2 thin films grown on c- and r-sapphire substrates”, J. Appl. Phys 107(5), 2010

[61] Z Yang and S Ramanathan, “Direct measurement of compositional complexity-induced electronic inhomogeneity in VO_2 thin films grown on gate dielectrics”, Appl. Phys. Lett. 98, 2011